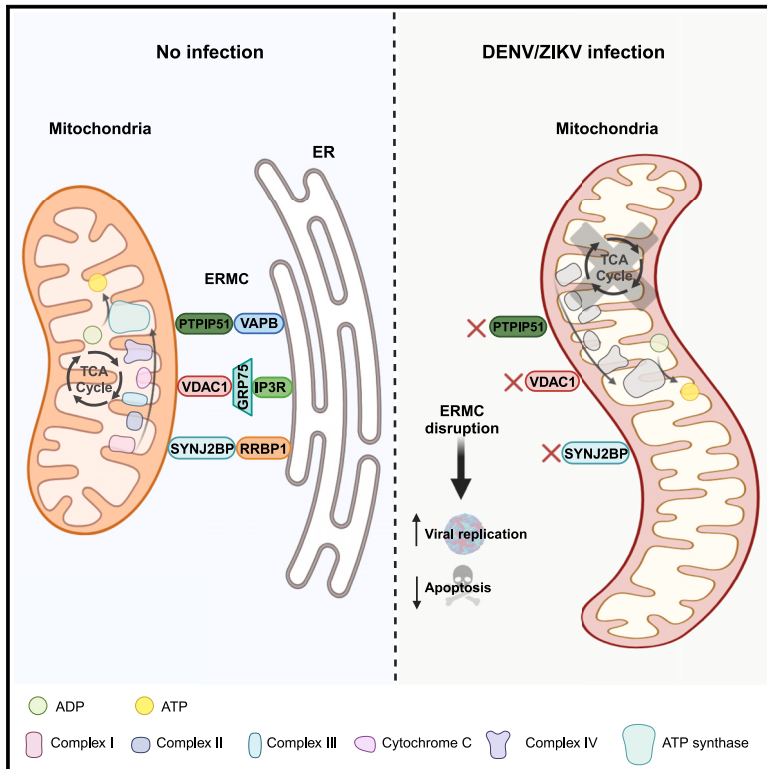# Dengue virus and Zika virus alter endoplasmic reticulum-mitochondria contact sites to regulate respiration and apoptosis

Graphical abstract

Authors

Wesley Freppel,
Viviana Andrea Barragan Torres,
Olus Uyar, ..., Pietro Scaturro,
Laura Hulea, Laurent Chatel-Chaix

Correspondence

laurent.chatel-chaix@inrs.ca

In brief

Virology; Mitochondria; Cell biology; Proteomics; Metabolomics

Highlights

- Dengue and Zika viruses alter endoplasmic reticulum-mitochondria contact sites (ERMC)

- Mitochondrial respiration is perturbed over the course of the infection

- ERMC protein knockdown increases viral replication

- ERMC proteins RRBP1 and SYNJ2BP regulate Zika virus-induced cell death

CellPress

iScience

Article

Dengue virus and Zika virus alter endoplasmic reticulum-mitochondria contact sites to regulate respiration and apoptosis

Wesley Freppel,[1,10] Viviana Andrea Barragan Torres,[1,11] Olus Uyar,[1,11] Anaïs Anton,[1,11] Zaynab Nouhi,[2] Mathilde Broquière,[1] Clément Mazeaud,[1] Aïssatou Aïcha Sow,[1] Alexanne Léveillé,[1] Claudia Gilbert,[1] Nicolas Tremblay,[1] Jonathan Eintrez Owen,[3] Cheyanne L. Bemis,[3] Xavier Laulhé,[1] Alain Lamarre,[1] Christopher J. Neufeldt,[3] Ian Gaël Rodrigue-Gervais,[1] Andreas Pichlmair,[4,5] Denis Girard,[1] Pietro Scaturro,[4,6] Laura Hulea,[2,7] and Laurent Chatel-Chaix[1,8,9,12,*]

[1]Centre Armand-Frappier Santé Biotechnologie, Institut National de la Recherche Scientifique, Laval, Québec H7V 1B7, Canada
[2]Maisonneuve-Rosemont Hospital Research Center, Montréal, Québec H1T 2M4, Canada
[3]Department of Microbiology and Immunology, Emory University School of Medicine, Atlanta, GA 30322, USA
[4]Institute of Virology, Technical University of Munich, School of Medicine 81675 Munich, Germany
[5]German Center of Infection Research (DZIF), Munich partner site, Munich, Germany
[6]Leibniz Institute of Virology 20251 Hamburg, Germany
[7]Department of Medicine, University of Montréal, Montréal, Québec H3C 3J7, Canada
[8]Center of Excellence in Orphan Diseases Research-Fondation Courtois, Québec, Canada
[9]Regroupement Intersectoriel de Recherche en Santé de l'Université du Québec, Québec, Canada
[10]Present address: Institute for Biomedicine and Glycomics, Gold Coast Campus, Griffith University, Southport, QLD 4222, Australia
[11]These authors contributed equally
[12]Lead contact
*Correspondence: laurent.chatel-chaix@inrs.ca
https://doi.org/10.1016/j.isci.2024.111599

SUMMARY

During infection, dengue virus (DENV) and Zika virus (ZIKV), two (ortho)flaviviruses of public health concern worldwide, induce alterations of mitochondria morphology to favor viral replication, suggesting a viral co-opting of mitochondria functions. Here, we performed an extensive transmission electron microscopy-based quantitative analysis to demonstrate that both DENV and ZIKV alter endoplasmic reticulum-mitochondria contact sites (ERMC). This correlated at the molecular level with an impairment of ERMC tethering protein complexes located at the surface of both organelles. Furthermore, virus infection modulated the mitochondrial oxygen consumption rate. Consistently, metabolomic and mitoproteomic analyses revealed a decrease in the abundance of several metabolites of the Krebs cycle and changes in the stoichiometry of the electron transport chain. Most importantly, ERMC destabilization by protein knockdown increased virus replication while dampening ZIKV-induced apoptosis. Overall, our results support the notion that flaviviruses hijack ERMCs to generate a cytoplasmic environment beneficial for sustained and efficient replication.

INTRODUCTION

(Ortho)flavivirus infections constitute a major public health concern worldwide. With an estimation of 390 million people infected per year, dengue virus (DENV) causes the most prevalent arthropod-borne viral disease.[1] Although DENV mainly circulates in (sub-)tropical regions, it has also now reached Europe and North America because of the vector colonization of these areas.[2,3] Upon infection through the bite of an *Aedes*-type mosquito, symptoms associated with dengue fever can manifest as severe fevers which may be hemorrhagic and eventually lead to plasma leakage-induced shock syndrome and death.[4] In 2015, Zika virus (ZIKV), another flavivirus closely related to DENV, quickly emerged in South America causing unexpected syndromes such as microcephaly in newborns following vertical transmission, in addition to other neurological complications in adults such as Guillain-Barré syndrome.[5,6] Unfortunately, no treatments against DENV and ZIKV are currently available, partly due to our limited knowledge of the cellular and molecular mechanisms involved in the flavivirus life cycle and pathogenesis, which could constitute therapeutic targets.

DENV and ZIKV are single positive-stranded RNA viruses belonging to the *Orthoflavivirus* genus within the *Flaviviridae* family. Following entry into the host cell, the viral RNA genome (vRNA) is translated into a single polyprotein at the membrane of the endoplasmic reticulum (ER). This viral protein product is cleaved by host and viral proteases, generating three structural proteins (C, prM, and E) which assemble with the vRNA to form new viral particles, and seven non-structural proteins (NS1, NS2A, NS2B, NS3, NS4A, NS4B, and NS5) which are

involved in the replication of the viral genome.[7] The viral replication takes place in cytoplasmic substructures called viral replication organelles (vRO) that are derived from ER membrane alterations induced by virus infection.[8–15] vROs comprise: 1- vesicle packets, believed to be the site of vRNA replication; 2- virus bags, ER cisternae in which immature assembled virions accumulate; and 3- convoluted membranes (CM), that are enriched in NS3, NS4B, and NS4A[13,16,17] whose functions are poorly understood. It was proposed that CMs dampen antiviral cellular processes, such as early innate immunity response and apoptosis to favor viral replication.

In DENV- and ZIKV-infected cells, mitochondria make physical contact with CMs and exhibit an elongated morphology, which stimulates viral replication.[16,18] This regulation of mitochondrial morphodynamics was attributed to NS4B which partly resides in CMs. The pharmacological destabilization of CMs induces mitochondria fragmentation and correlates with the stimulation of virus-induced apoptosis.[19] Conversely, mitochondria elongation positively influences the size and abundance of CMs and dampens the RIG-I-dependent type-I and -III interferon induction.[16] This supports a model in which flaviviruses regulate mitochondrial functions through their contacts with CMs for the benefit of replication. There have been several conflicting reports about the impact of flavivirus infection on mitochondrial respiration,[18,20–23] which may be explained by the use of different cell models, the time of infection, or their susceptibility to induce innate immunity and cell death upon stress. This results in challenges to analyze the phenotypes, especially regarding the contribution of interferon. Thus, a kinetic analysis of the respiration of infected cells over the course of infection in an interferon-free context is lacking so far.

ER-mitochondria contact sites (ERMC) rely on protein-protein connections maintaining a 10-25 nm-wide interface between the ER and the mitochondria that allows transfers of molecules between both organelles.[24–26] This ultrastructure contributes to several cellular processes such as calcium homeostasis, lipid transport, autophagy regulation, mitochondrial morphodynamics, apoptosis induction, and early innate immunity.[27–31] Illustrating their important roles in cellular processes, ERMCs are a target of viruses (such as hepatitis C virus, cytomegalovirus and influenza virus) for interfering with mitochondrial-mediated antiviral responses.[32–35] Interestingly, treatment of cells with Mito-C, a compound that induces both mitochondrial fission and the formation of ERMCs did inhibit DENV replication.[36] Recently, we have shown that DENV-induced mitochondria elongation positively regulates the biogenesis of CMs.[16] This was accompanied by a decrease in colocalization between the ER and mitochondria at the cellular level in confocal microscopy with a resolution that did not allow us to discriminate between organelles in close contacts from those in proximity. However, while there was some evidence of the loss of ERMC in electron microscopy,[16] it is still unknown whether DENV and other flaviviruses such as ZIKV globally alter ERMCs and what the resulting impacts are regarding cellular processes such as oxidative respiration and apoptosis.

In this study, we show an overall alteration of the ERMC compartment following DENV and ZIKV infections. Concomitantly, reducing the expression of several ERMC proteins

responsible for tethering mitochondria and the ER increased DENV and ZIKV replication, supporting that both viruses alter ERMC to stimulate viral replication. Interestingly, the expression profile of several ERMC proteins was changed with a drastic decrease in the levels of RRBP1 over the course of the infection and the appearance of an alternative ZIKV-specific SYNJ2BP protein product. This suggests that both viruses destabilize ERMC by targeting tethering proteins. Furthermore, both DENV and ZIKV modulated mitochondrial respiratory metabolism in living cells. This correlated with a decrease in the abundance of several metabolites of the Krebs cycle and changes in the stoichiometry of the electron transport chain. Most importantly, targeting ERMC by silencing either RRBP1 or SYNJ2BP increased respiration and dampened ZIKV-induced apoptosis supporting the importance of ERMC alteration by DENV and ZIKV for attenuating antiviral cellular processes and for maintaining a cytoplasmic environment favorable to the viral replication.

RESULTS

DENV and ZIKV alter endoplasmic reticulum-mitochondria contact sites

Previous observation of DENV-infected Huh7 cells at the ultrastructural level suggested that ERMCs were altered. Although this was not quantified, this correlated with a decrease of 3D colocalization between mitochondria and ER in a limited number of analyzed cells in confocal microscopy, i.e., at a resolution which is too low to precisely detect and measure heterotypic organelle contacts.[16] The molecular mechanism underlying this phenotype was not described and it was also not established whether this phenotype is specific for DENV or also expands to other relevant flaviviruses, such as ZIKV. To clearly address whether DENV and ZIKV infections induce a global alteration of ERMCs, we carried out a comprehensive quantitative ultrastructural analysis of DENV- and ZIKV-infected Huh7.5 hepatoma cells using transmission electron microscopy. In order to ensure that any observed phenotype is not caused by early innate immune activation, a process that relies on mitochondrial protein MAVS, the Huh7.5 cell line was chosen as a model because these cells are defective in RIG-I-dependent interferon induction which is the primary immune pathway involved in DENV sensing.[16,37,38] Replication kinetic experiments in Huh7.5 cells (Figure S1A) established that the peak of DENV (serotype 2 strain 16681s) and ZIKV (contemporary strain H/PF/2013) particle production was achieved at 2 days post-infection (dpi) as monitored by plaque assays. Moreover, ZIKV replicated more slowly than DENV in this cell line and a higher multiplicity of infection (MOI) was required for ZIKV to achieve a percentage of infection close to 100% at this time point (Figure S1A). As a result, to maximize the number of infected cells at 2 dpi for imaging, we have used MOIs of 1 and 10 for infections with DENV and ZIKV, respectively. Consistent with our previous studies in Huh7 cells,[16] we have also confirmed that with these selected MOIs, the proportion of infected Huh7.5 cells exhibiting elongated mitochondria increased over the course of the infection with a more marked phenotype with DENV than with ZIKV (Figures S1B and S1C). Subsequently, more than two hundred mitochondria per conditions (n = 215–351) were analyzed for ERMCs in single sections

of cells using transmission electron microscopy following 48 h of infection with the ZIKV H/PF/2013 or DENV 16681s. In uninfected conditions, 74.7% of mitochondria were surrounded by ER tubules with up to 75% of the mitochondrial perimeter being in contact with these ER membranes (median at 31.4%; Figures 1A–1C). In stark contrast, both DENV and ZIKV-infected cells exhibited a reduced proportion of mitochondria in contact with ER membranes, with a phenotype more pronounced for DENV than for ZIKV. In addition, when the two organelles were still physically associated, only 19% of the mitochondria perimeter in average were in contact with ER following both ZIKV and DENV infections, compared to 35% in uninfected condition (Figure 1C). Consistent with the previous observation, mitochondria showed an elongated morphology and were often located in the vicinity of CMs (Figure 1A).

To examine the impact of both virus infections on ERMCs at a molecular level in a larger cell population, we analyzed the extent of protein-protein interactions involved in tethering mitochondria and ER using proximity ligation assay (PLA). This technique allows the detection of the proximity between two proteins at a maximum distance of 40 nm and the analysis of the intracellular localization of protein complexes using confocal microscopy. We focused our PLA analysis on three ERMC tethering complexes known to contribute to ERMC formation and/or stability, namely the interactions between: 1- ER resident vesicle-associated membrane protein-associated protein B (VAPB) and the mitochondrial outer membrane protein, protein tyrosine phosphatase-interacting protein 51 (PTPIP51, also named RMDN3)[39]; 2- ER resident ribosome-binding protein 1 (RRBP1) and the mitochondrial protein synaptojanin 2-binding protein (SYNJ2BP)[40,41]; and 3- the ER protein inositol 1,4,5-trisphosphate receptor 1 (IP3R1) and mitochondrial voltage-dependent anion-selective channel 1 (VDAC1) via the chaperone glucose-regulated protein 75 (GRP75)[42] (Figure 2A). First, we confirmed that PLA signals detected for these three different tethering complexes mostly colocalized with the mitochondria network in Huh7.5 cells stably expressing the mitochondria-localized mito-mTurquoise2 fluorophore (Figure S2A). Second, PLAs involving non-interacting ERMC proteins VAPB and SYNJ2BP1 resulted in much less signal than that for RRBP1-SYNJ2BP association, highlighting the specificity of complex detection even though these proteins are all present in the reticulo-mitochondrial interface (Figure S2B). PLAs were then performed for RRBP1-SYNJ2PB, VAPB-PTPIP51 and IP3R1-VDAC1 interactions in uninfected- or DENV/ZIKV infected-Huh7.5 cells at 2 and 3 dpi and combined with the immunostaining of NS3 viral protein to identify infected cells. As expected, we detected a high amount of RRBP1-SYNJ2BP (Figure 2B), VAPB-PTPIP51 (Figure 2C) and IP3R1-VDAC1 (Figure S2C) interactions in the uninfected condition in confocal microscopy. These signals were specific to the targeted protein-protein interactions since omitting either primary antibody gave very little, if any, PLA signal (Figure 2D, see Ab alone controls). Strikingly, when comparing ZIKV- or DENV-infected (green) and uninfected cells in the same images, it was obvious that the RRBP1-SYNJ2BP PLA signal was less abundant in infected cells (Figure 2B). Subsequent quantification of the PLA dots per cell demonstrated an overall decrease in PLA signal in NS3-positive cells (i.e., infected) in all three assays (Figures 2D and S2C) which was particularly marked

for ZIKV at 48 h post-infection (hpi). For DENV, this phenotype appeared later compared to ZIKV since the signal reduction became significant at 72hpi for RRBP1-SYNJ2BP and IP3R1-VDAC1 interactions. Overall, these data demonstrate a decrease in the abundance of the RRBP1-SYNJ2BP, IP3R1-VDAC1 and VABP-PTPIP51 ERMC tethering complexes and confirm an alteration of ERMCs by DENV and ZIKV at the molecular level. Interestingly, this decrease was particularly prominent for RRBP1-SYNJ2BP and IP3R1-VDAC1 at 3 dpi. Confirming these results in other cell lines, the abundance of PLA signals for RRBP1-SYNJ2BP complexes was also reduced in both trophoblastic JEG-3 cells and lung adenocarcinoma A549 cells infected with DENV or ZIKV compared to the uninfected control (Figure S3).

To examine the impact of DENV and ZIKV infection on the expression of ERMC proteins, we performed western blotting on extracts from uninfected or infected Huh7.5 cells at 2 and 3 dpi. The expression levels of GRP75, VDAC1, VAPB and PTPIP51 remained mostly unchanged upon ZIKV and DENV infections (Figures S4A and S4B). In contrast, the expression of RRBP1 was reduced at 48 h post-infection with a further decrease of its levels at 72hrs post-infection (Figures 3A and S4A). Moreover, an alternative SYNJ2BP product exhibiting a higher molecular weight was detected in ZIKV-infected cells at 48 and 72 h post-infection (Figures 3A and S4A). Finally, our immunofluorescence-based confocal microscopy analysis of DENV- and ZIKV-infected cells did not reveal any major changes in the sub-cellular distribution of IP3R1, VDAC1, RRBP1, SYNJ2BP and PTPIP51 in DENV/ZIKV infection (Figures S5 and 3B). Interestingly, viral infection induced a drastic relocalization of ER-resident VAPB into large NS3-positive foci reminiscent of CMs (Figure 3B), suggesting that DENV and ZIKV alter VAPB/PTPIP51-dependent ERMC by physically sequestering VAPB. Altogether, these data strongly support that DENV and ZIKV target ERMC tethering complexes.

DENV and ZIKV perturb mitochondrial respiration

The remodeling of organelles such as ER or mitochondria by flaviviruses and maintaining vROs is presumably highly energy-consuming while being a source of cellular stress. Considering that mitochondria is the powerhouse of the cell, we investigated the impact of flaviviral infection on the oxidative respiration process in mitochondria, which is the main source of energy in the form of adenosine triphosphate (ATP) in cells. Briefly, we analyzed mitochondrial respiration properties in living uninfected and infected Huh7.5 cells at 24, 48 and 72 h post-infection by measuring the oxygen consumption rate (OCR) while sequentially adding oligomycin (ATP synthase inhibitor), FCCP (protonophore) and rotenone/antimycin A (complex I and III inhibitors, respectively) that directly act on the electron transport chain of the inner mitochondrial membrane (Figure 4A). The OCR profile, an indicator of mitochondrial respiration was normalized to the mean basal OCR in the uninfected conditions in each independent experiment. The OCR slightly increased at 24 h post-infection with both viral infections compared to the uninfected condition (Figures 4B and 4E). Very interestingly, the OCR profiles were shifted down at later time points of the infection at levels attributed to the non-mitochondrial oxygen consumption (Figures 4C–4E) suggesting that mitochondria are no longer
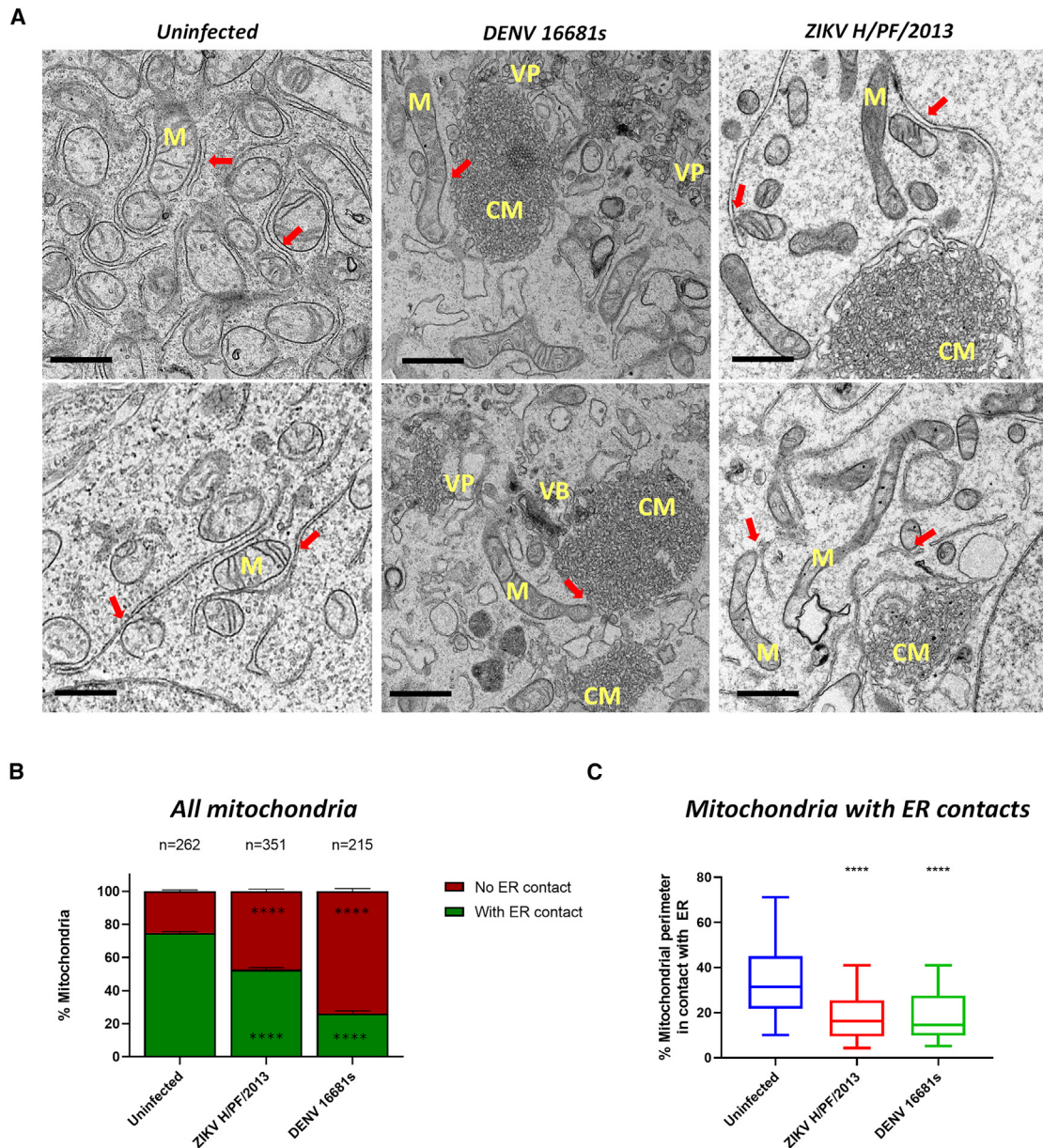
Figure 1. DENV and ZIKV infection alter endoplasmic reticulum-mitochondria contact sites

Huh7.5 cells were infected with DENV 16681s (multiplicity of infection (MOI) = 1), or ZIKV H/PF/2013 (MOI = 10) or left uninfected. Forty-eight hours later, cells were processed for transmission electron microscopy.

(A) Electron micrographs of uninfected and infected cells. Red arrows indicate ER-mitochondria contact sites. CM: convoluted membranes; VP: vesicle packets; M: mitochondria; VB: virus bags. Scale bar = 1 μm.

(B) Proportion of mitochondria with or without contacts with the ER; n = number of mitochondria analyzed per condition. ****: $p \leq 0.0001$; two-way ANOVA test.

(C) Percentage of the mitochondrial perimeter in contact with ER. The mitochondria of (B) which were not in contact with ER were excluded from this quantification. Values in the 5%–95% percentile range are shown. Analyses were made with micrographs from 2 independent infection experiments (54–197 mitochondria per condition). ****: $p \leq 0.0001$; Kruskal-Wallis test.

able to efficiently perform oxidative respiration. Analyzing the OCR profiles revealed increases in the basal respiration, the ATP-linked respiration, and the maximal respiration at 24 h post-infection whereas a drastic significant shut-off of these indicators was observed at 72 h post-infection demonstrating a

time-dependent modulation of the oxidative respiration by flaviviruses. (Figure 4E).

To gain more insight about the causes of this respiration alteration at the late time points of flaviviral infection, we analyzed the mitochondrial levels of proteins involved in the Krebs cycle and
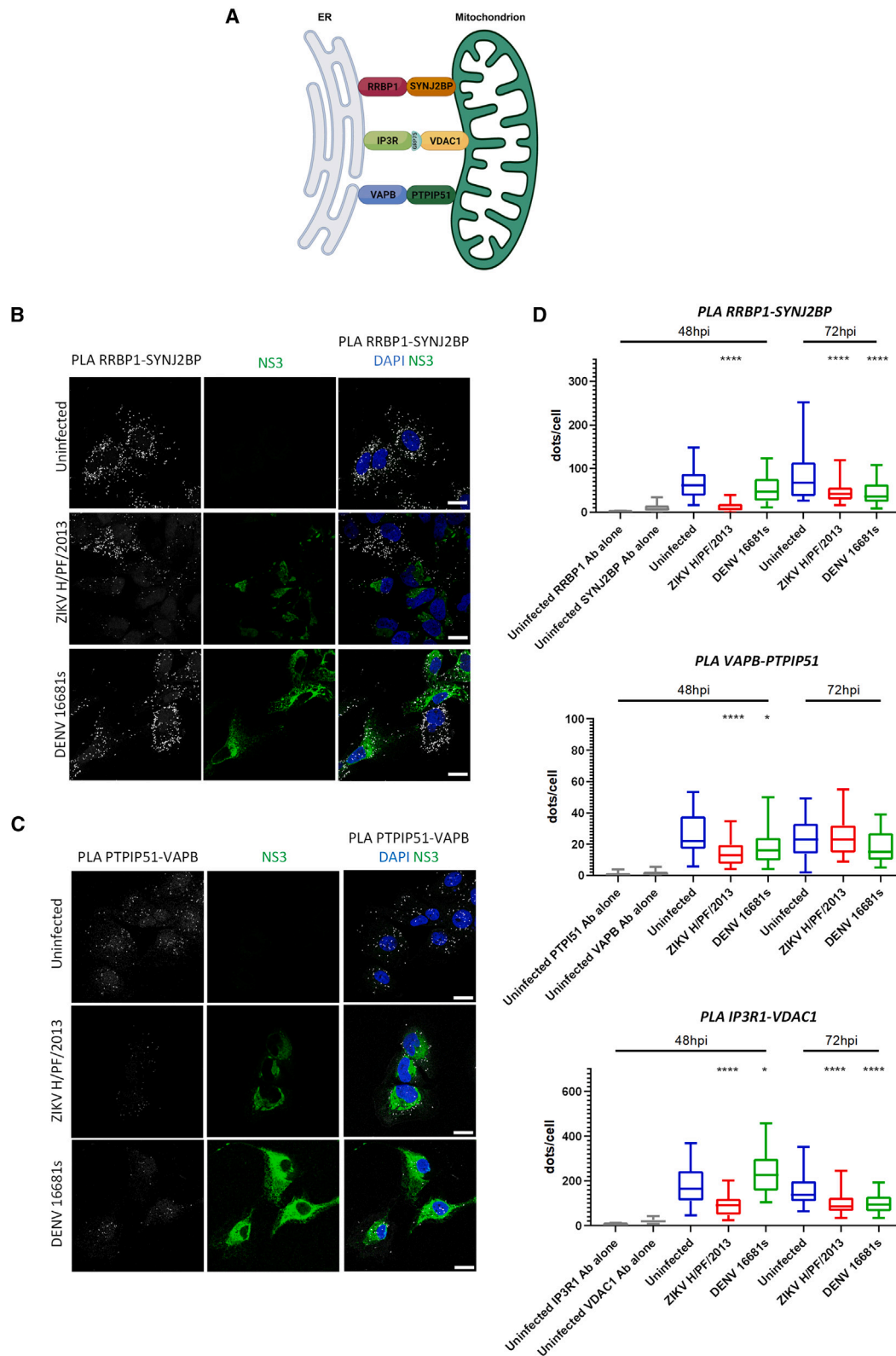
the electron transport chain (ETC) by performing quantitative mass spectrometry on mitochondria purified from uninfected and ZIKV- and DENV-infected-Huh7.5 cells at 48 h post-infection. We have included in the analysis a second ZIKV strain from the African lineage, namely MR766. This mitoproteomic analysis identified changes in the stoichiometry of several proteins of the ETC proteins compared to uninfected cells (Figures 4F and 4G and Table S1). Most notably, the composition of the complex II (succinate dehydrogenase), which is a component of both the Krebs cycle and the ETC was changed upon infection. Indeed, mitochondrial levels of sub-units D and C of SDH were increased upon DENV and ZIKV MR766 infections, respectively, compared to other subunits. Interestingly, the SDH assembly factor SDHAF2 was less abundant in mitochondria from DENV-infected cells and this phenotype was confirmed by western blotting on purified mitochondria (Figure S6A). However, in contrast to SDH, the mitochondrial levels of all other enzymes of the Krebs cycle remained unchanged (Figure 4G and Table S1). The changes in SDH composition correlated with a drastic decrease of several metabolites of the Krebs cycle (i.e., α-ketoglutarate/succinate for the two ZIKV strains, and fumarate/malate for all tested viruses) as measured by gas chromatography-coupled mass spectrometry (GC-MS) (Figures 4G and S6B). Interestingly, in the case of DENV infection, the levels of citrate and *cis*-aconitate were specifically increased, which suggests a dysfunction of the Krebs cycle downstream aconitase activity. In addition to complex II, the stoichiometries of complexes I, III and IV were also altered in DENV- and ZIKV-infected cells with COX6C, COX7A2, COA4 and NDUFS4 being modulated by all three tested flaviviruses (Figures 4F and 4G and Table S1). In contrast, some modulated ETC proteins were specific to either virus (Figure 4F). Flow cytometry analysis of infected cells with MitoTracker Orange showed that DENV and ZIKV did not induce a notable decrease in the mitochondrial potential at 48 hours post infection (Figure S6C). This strongly supports that the observed respiration and mitoproteome phenotypes were not the result of a loss of mitochondrial integrity at that time point. Altogether, these data combining respirometric, proteomic and metabolomic approaches clearly demonstrate that ZIKV and DENV interfere with the mitochondrial respiratory metabolism.

Endoplasmic reticulum-mitochondria contact site alteration increases mitochondrial respiration

Since DENV and ZIKV infections induce a shut-off of the mitochondrial oxygen consumption over time and disrupt ERMCs, we investigated the impact of the alteration of this sub-cellular compartment on respiration. To that aim, we analyzed the oxygen consumption of living cells following expression knockdown of ERMC tethering proteins by transducing cells with shRNA-expressing lentiviruses. Indeed, it is well established that knockdown of ERMC proteins destabilizes physical contacts between ER and mitochondria organelles.[43–46] We identified short hairpin RNAs (shRNA) whose expression led to efficient silencing of SYNJ2BP, RRBP1, VAPB and PTPIP51 without reducing cellular viability 4 days post-transduction (Figures S7A and S7B). The IP3R1-GRP75-VDAC1 tethering complex was voluntarily omitted from the analysis because we reasoned that knocking these factors down may induce pleiotropic effects related to their ion channel activity and their role in calcium homeostasis and not to the contacts *per se*.[42] To exclude the possibility that potential phenotypes would be due to changes in mitochondrial morphodynamics (which can influence viral replication),[16,18] we used confocal microscopy to control that ERMC protein knockdown did not change the morphology of the mitochondrial network compared to the non-target shRNA (shNT) control condition (Figure S7D). As control, knockdown of fission factor DRP1 and fusion factor MFN2 led to mitochondrial elongation and fragmentation, respectively (Figures S7A and S7D). Moreover, flow cytometry analysis of ERMC protein-depleted cells showed no impact of ERMC alteration on the mitochondrial potential (Figure S7C). Interestingly, the respiration in Huh7.5 cells in which ERMC proteins were knocked down globally increased as compared to the shNT control condition (Figures 5A–5C). This trend was observed for the basal, maximal and ATP-linked mitochondrial oxygen consumption rates although this was not always statistically significant for all parameters and tested shRNAs. In contrast, no obvious changes in the OCR parameters were observed when mitochondrial morphodynamics was modulated upon DRP1 and MFN2 knockdown. These data indicate that ERMC alteration by DENV and ZIKV stimulates respiration independently of mitochondria morphodynamics and may explain why respiration is increased at early time points. Such a viral regulation might also attenuate the respiratory stress induced later in the infection.

Endoplasmic reticulum-mitochondria contact protein knockdown increases viral replication

We next investigated the impact of the RNAi-mediated alteration of ERMCs on viral replication. Huh7.5 cells in which ERMC proteins were knocked down were infected with a DENV reporter virus (DENV-R2A) expressing *Renilla reniformis* luciferase (Rluc), allowing us to evaluate DENV replication levels by measuring bioluminescence in cells at 2 days post-infection. We observed an increase in DENV-R2A replication upon ERMC protein knockdown, which was more pronounced when VAPB and PTPIP51

Figure 2. DENV and ZIKV infection decrease the interactions between ERMC proteins

(A) Schematic representation of ERMC tethering complexes. Created with BioRender.com.

(B and C) Huh7.5 cells were infected with DENV 16681s (MOI = 1) or ZIKV H/PF/2013 (MOI = 10) or left uninfected. Two or three days later, cells were fixed and subjected to proximity ligation assays (PLA) to detect (B) SYNJ2BP-RRBP1 or (C) VAPB-PTPIP51 interactions, and immunostained for NS3 viral protein to identify infected cells. Cells were imaged using confocal microscopy. Representative images are shown. Scale bar = 20 μm.

(D) Quantification of PLA dot abundance for RRBP1-SYNJ2BP, VAPB-PTPIP51, and IP3R1-VDAC1 interactions in uninfected- and infected cells from two independent experiments. Values in the 5%–95% percentile range are shown. ****: $p \leq 0.0001$; *: $p \leq 0.05$; Kruskal-Wallis test for all except for RRBP1-SYNJ2BP 72hpi dataset (normal distribution of the data for the three conditions), which was analyzed with a one-way ANOVA test. Between 40 and 90 cells per condition over 2 independent experiments were analyzed. The "Ab alone" specificity controls were not taken into account for the statistical analysis.
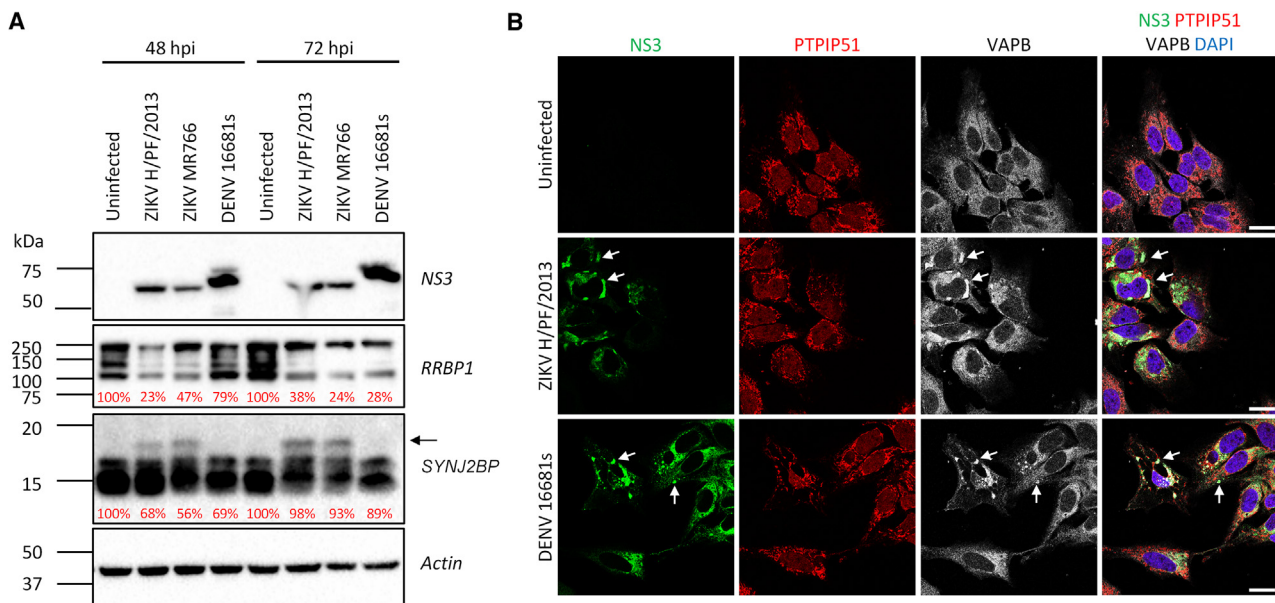
Figure 3. Flaviviruses modify the intracellular distribution of VAPB and the expression profiles of RRBP1 and SYNJ2BP

(A) Huh7.5 cells were infected with DENV 16681s (MOI = 1) or ZIKV H/PF/2013 (MOI = 10) or left uninfected. 48 or 72 h post-infection, cell extracts were prepared, and the expression levels of the indicated proteins were analyzed by western blotting. The arrow indicates the ZIKV-induced SYNJ2BP protein product. Protein expression levels relative to uninfected control and normalized to actin are indicated in red.

(B) Cells were infected as in (A) and were imaged at two days post-infection by confocal microscopy using antibodies detecting VAPB and PTIP51. Infected cells were detected with anti-NS3 antibodies. Scale bar: 20 μm.

were depleted (Figure 5D). Consistently, comparable phenotypes were obtained when cells were infected with either wild-type DENV2 16681s or ZIKV H/PF/2013 since the production of infectious viral particles as measured by plaque assays was increased upon knockdown of ERMC proteins (except for the shPTPIP51/DENV condition; see discussion) (Figures 5E and 5F). As controls and in line with previous observations,[16] the modulation of mitochondrial morphodynamics showed the expected phenotypes. Indeed, the silencing of DRP1, which results in enhanced mitochondrial elongation, stimulated DENV replication while the reduction of MFN2 expression impaired it (Figures 5D and 5E). Most importantly, RRBP1 and SYNJ2BP knockdown resulted in increased replication of both DENV and ZIKV in human primary monocytes isolated from two healthy donors (Figures 5G and 5H). As a control condition, monocyte treatment with the NS5 RNA polymerase inhibitor NITD008[47,48] decreased vRNA levels, demonstrating a productive replication in these primary cells. Overall, these data indicate that ERMC proteins restrict viral replication and further support that the DENV- and ZIKV-induced modulation of the physical contacts between mitochondria and ER is proviral.

RRBP1 and SYNJ2BP regulate ZIKV-induced apoptosis

We have previously shown that CM integrity relies on VCP ATPase activity which is required to dampen ZIKV-induced apoptosis.[19] Since CMs are physically connected to mitochondria through residual associated ER membranes and considering that ERMC were reported to regulate mitochondria-dependent cell death,[49–52] we hypothesized that the alteration of

ERMC integrity dampens apoptosis during flaviviral infection. To test this, we measured the activity of caspase 3 (the major regulator of the execution phase of apoptosis) in Huh7.5 cells upon RRBP1 or SYNJ2BP silencing. We chose this ERMC tethering couple since it was the most impacted by ZIKV infection (Figure 2). Very interestingly, upon RRBP1 or SYNJ2BP depletion, the activity of caspase 3/7 was reduced in lysates of ZIKV-infected cells as measured using a bioluminescence-based assay (Figure 6A). We confirmed these phenotypes by flow cytometry using the CellEvent caspase-3/7 green reagent, a fluorescent biosensor of caspase 3/7 activity, and anti-NS3 antibodies to detect ZIKV-infected cells (Figure 6B). While 61.8% of the cells were apoptotic (i.e., CellEvent-positive) in control infected conditions (shNT), this proportion was reduced to 13.2% and 15.3% when RRBP1 and SYNJ2BP were knocked down, respectively. Moreover, the proportion of ZIKV infected cells which were non-apoptotic (i.e., NS3-positive/CellEvent-negative cells) drastically increased under these conditions (13.8% for shNT versus 59.7% and 49.6% for shRRBP1 and shSYNJ2BP, respectively). Furthermore, by combining these markers with the amine reactive viability dye LIVE/DEAD aqua fixable stain (Figure 6C), we showed that the silencing of RRBP1 and SYNJ2BP decreased the proportion of dead ZIKV-infected cells, namely cells that were apoptotic and exhibited a ruptured plasma membrane (% of NS3-gated CellEvent-positive and LIVE/DEAD-positive cells; Figure 6C). Finally, as expected, no apoptosis was observed in any uninfected conditions demonstrating that ERMC destabilization *per se* does not induce apoptosis (Figure 6B). In contrast, as positive control, treatment
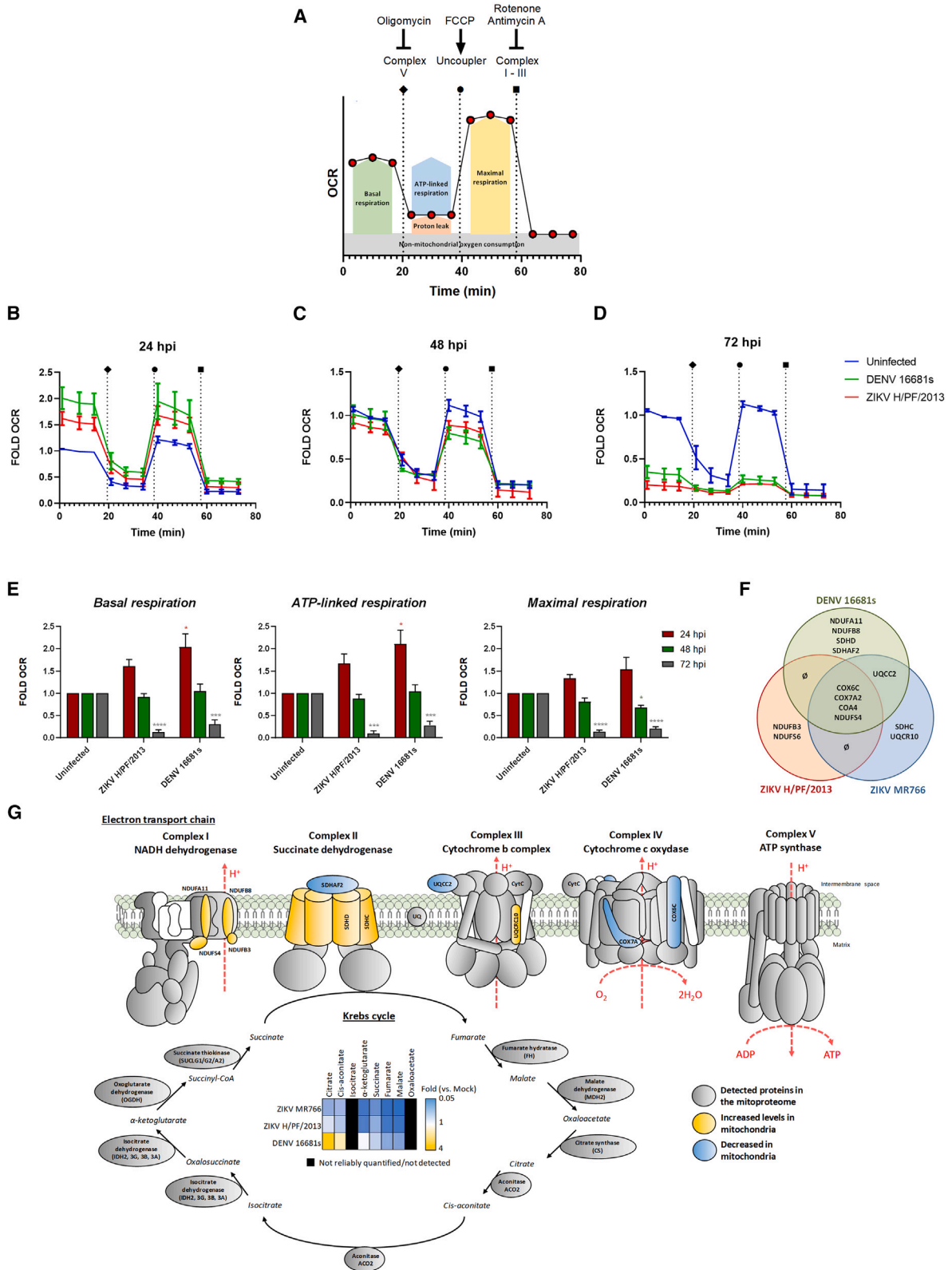
(legend on next page)

of the cells with actinomycin D robustly induced apoptosis. Altogether, these data support that ZIKV alters ERMC integrity to dampen infection-induced apoptosis and promote replication.

DISCUSSION

In this study, we demonstrate that DENV and ZIKV modulate the mitochondrial oxidative respiration and virus-induced apoptosis in favor of viral replication notably by altering the physical contacts between mitochondria and the ER. Our observations are consistent with the fact that ERMCs were reported to play a crucial role in the induction of the apoptosis pathway.[49–52] Such morphological remodeling allows flaviviruses to create a proviral cytoplasmic environment. This is in line with the fact that DENV replication is impaired when cells are treated with Mito-C, a drug that induces both mitochondrial fission and ERMC formation.[36] Although there is reported evidence that mitochondrial fission can be initiated at sites where the ER tubules wrap mitochondria and constrict mitochondria prior to DRP1 recruitment,[30] we did not observe any changes in mitochondria morphology upon ERMC protein knockdown in Huh7.5 cells (Figure S7D) supporting that the phenotypes reported here are independent of DRP1-mediated fission regulation by flaviviruses.[16,18]

Flavivirus infections induce the formation of membranous replication factories from the ER membranes.[8,9] More recently, it was shown that DENV and ZIKV induce the elongation of mitochondria in the vicinity of CMs.[16,18] Consistent with previous observations,[16] we noticed that mitochondria remain connected to CMs via residual associated ER membranes. This raises the hypothesis that the morphogenesis of CMs uses the reticulo-mitochondrial interface as a source of ER membranes via the destabilization of this specific cytoplasmic compartment. In addition, we show that DENV and ZIKV alter ERMCs by decreasing the abundance of three different tethering protein complexes (RRBP1-SYNJ2BP, IP3R1-VDAC1 and VAPB-PTPIP51). We did not observe any difference in the expression level of VDAC1, VAPB, and PTPIP51. Interestingly, RRBP1 levels were reduced after 48 h of infection with both viruses while a ZIKV-specific SYNJ2BP product exhibiting a higher molecular weight was detected. Whether this results from a flavivirus-specific regulation of alternative splicing or of posttranslational modifications will be explored in future studies. While VAPB-PTPIP51 and IP3R1-VDAC1 were reported to contribute to calcium homeostasis, autophagy and phospholipid transfer,[39,53–55] the contribution of the RRBP1-SYNJ2BP complex to specific cellular function beyond contributing to ERMCs is unknown.[56] This could explain why DENV and ZIKV specifically target this protein-protein couple to separate ER and mitochondria without affecting essential cellular processes. Interestingly, RRBP1 was recently shown to regulate ER morphology under cell starvation.[56] While this raises the possibility that RRBP1 regulates the formation of ER-derived vROs, our preliminary data using a replication-independent vRO induction system (pIRO-Z)[57] showed that RRBP1 and SYNJ2BP knockdown did not impact the de novo biogenesis of vesicle packets. However, we cannot exclude a role of ERMC in CM morphogenesis or virion assembly. In addition, MIGA2 and ESYT1, two proteins also regulating ERMCs via their binding to VAPB and SYNJ2BP, respectively[58,59] might also be part of this process. The putative targeting of MIGA2/VAPB complex by DENV (instead of PTIPI51/VAPB) could explain in that case why the knockdown of PTPIP51 did not stimulate wild-type DENV production (although it did for the reporter virus for reasons we cannot explain; Figure 5D–5E). Moreover, our ERMC cellular distribution analysis using confocal microscopy (Figures 3A and S5) showed that in some infected cells, VAPB relocalized to NS3-positive structures which are reminiscent of CMs while this was not observed for RRBP1, another ER-resident protein. It is thus tantalizing to speculate that flaviviruses sequester VAPB in these large virus-induced ER-derived structures to modulate the functions of the VAPB-PTIP51 tethering complex in autophagy and lipid and calcium transfer to mitochondria.[39,54,55] Notably, Gomez-Suaga has reported that VAPB-PTIP51-mediated ERMCs negatively regulate the formation of autophagosomes. Considering that autophagy is required for the efficient replication of both DENV and ZIKV,[60] it will be relevant to investigate whether the disruption of VAPB-PTPI51 tethering complexes by ZIKV and DENV promotes this proviral cellular process.

Interestingly, a recent mass spectrometry-based study has shown that in human fibroblasts, herpes simplex virus type 1, influenza A virus and betacoronavirus HCoV-OC43 infections decrease the abundance of mitochondrial proteins involved in ERMC whereas the human cytomegalovirus (HCMV) infection

Figure 4. DENV and ZIKV perturb mitochondrial respiration

Huh7.5 cells were infected with DENV 16681s (MOI = 1) or ZIKV H/PF/2013 (MOI = 10), or left uninfected for 24, 48 and 72h before analysis.

(A) Schematic representation of the respiration profile in living cells generated with the Seahorse technology. The ATP synthase inhibitor oligomycin, the proton ionophore carbonyl cyanide *p*-trifluoromethoxyphenylhydrazone (FCCP), and a mixture of mitochondrial complex III inhibitor antimycin A/mitochondrial complex I inhibitor rotenone are sequentially added to analyze various parameters of the respiration.

(B–D) The oxygen consumption rates (OCR) of uninfected and infected cells were measured at the indicated time points and were normalized to the mean of the basal OCR in the uninfected condition for each independent experiment. The mean normalized OCR from five experiments is shown.

(E) Based on the data of (3b-d), basal respiration, ATP production, and maximal respiration were determined. ****: $p \leq 0.0001$; ***: $p \leq 0.001$; *: $p \leq 0.05$; one-way ANOVA test ($N = 3$).

(F–G) DENV/ZIKV-infected and control cells were analyzed two days post-infection for their mitochondrial protein composition following mass spectrometry on purified mitochondria ($N = 4$), as well as for the abundance of the Krebs cycle metabolites measured by GC-MS in 4 independent experiments.

(F) A Venn diagram illustrating the electron transport chain proteins whose mitochondrial abundance was significantly changed when cells are infected with DENV 16681s, ZIKV H/PF/2013 or ZIKV MR766. (G) Schematic representation of the mitochondrial electron transport chain coupled to the Krebs cycle is shown. Blue elements indicate proteins/metabolites that were downregulated upon DENV/ZIKV infection. In contrast, yellow elements highlight upregulated proteins/metabolites. The expression of the proteins in gray were not significantly impacted by flaviviral infections. All values were normalized to the uninfected condition. Isocitrate and oxaloacetate were not detected using GC-MS in these experiments.
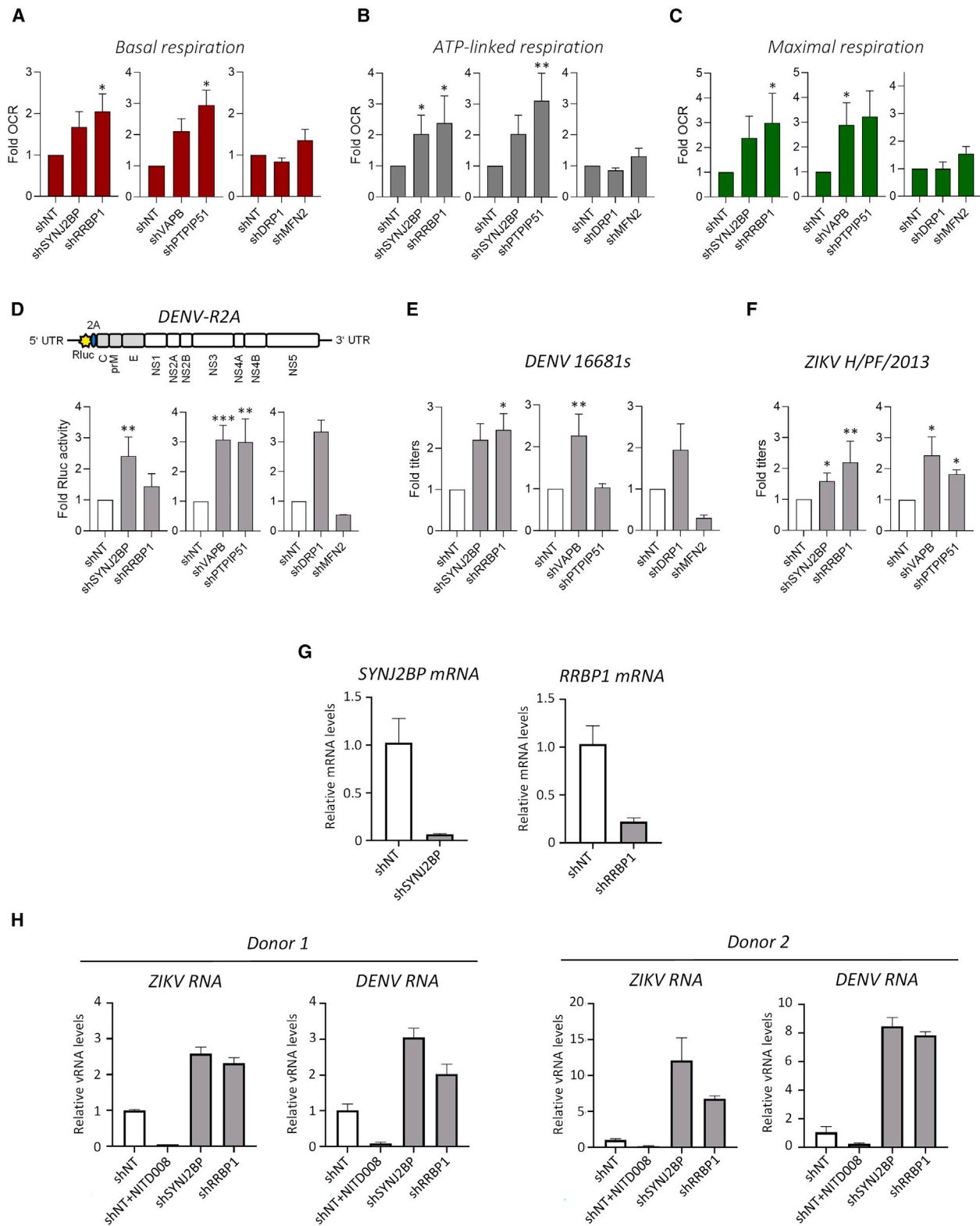
Figure 5. ERMC proteins negatively regulate mitochondrial respiration and viral replication

(A–C) Huh7.5 cells were transduced with lentiviruses expressing shRNAs which target the indicated proteins (MOI = 4). Four days later, cells were trypsinized, counted, and processed for measurements of various parameters of the oxygen consumption rate using the Seahorse technology as described in the STAR

(legend continued on next page)

primarily increased ERMC protein levels.[34] Increasing the abundance of ERMC proteins such as VAPB, MFN1/2 fusion proteins, fission-associated proteins DRP1 and MFF, and ER-mediated calcium transfer proteins PTPIP51 and VDAC1 occurred very early during the infection (8 h post-infection). This HCMV-mediated regulation of ERMCs favors cellular processes such as ER-to-mitochondria calcium flux, mitochondrial fragmentation, and reshaping of the cristae for the benefit of HCMV particle production. In line with the study mentioned above, a prior work showed that influenza virus infection also alters ERMCs and induces mitochondria elongation to promote replication.[35] This highlights that viruses from families other than *Flaviviridae* have evolved to co-opt mitochondrial functions via diverse strategies.

The biogenesis of vROs is initiated early in infection and their maintenance presumably requires high energy levels in the form of ATP. Consistently, we show here that in the first 24 h of infection, DENV and ZIKV infections significantly increase the oxidative respiration followed by a near complete shut-down of this bioenergetic process later in the infection, which correlated with a decrease in the levels of several metabolites of the Krebs cycle (Figures 4 and S6B). This might result from the mitochondrial stress and the onset of cytopathic effects generated by the accumulation of ER-associated viral proteins over the course of the infection. The close analysis of oxygen consumption rate profiles using the Seahorse technology with different inhibitors of the ETC revealed that global respiration was impacted by DENV and ZIKV rather than only the maximal respiration for instance. In line with our data, a recent study showed increases in oxygen consumption and ATP production in astrocytes at the early time points of the infection (i.e., 18 to 24 h post-infection).[22] In contrast, later in the infection, the phenotype was reversed with an observed decrease in oxygen consumption at 48 h post-infection. These data support our model of high energy needs when DENV and ZIKV establish the infection notably during the biogenesis of vROs. It is worth mentioning that some studies reported contrasting phenotypes. For instance, it was reported that DENV infection increases oxidative respiration in Huh7 and HepG2 liver cells at 2 days post-infection.[18,20] Other studies showed an inhibition of the basal and maximal oxygen consumption in first-trimester primary trophoblasts and fetal lung fibroblasts infected with ZIKV, that correlated with the fragmentation of the mitochondrial network.[21,23] In neurons, ZIKV infection also induced mitochondrial fission by decreasing the expression of the fusion factor MFN2 despite low levels of viral replication.[61] Pharmacological inhibition of DRP1 (and hence,

of fission) reduced ZIKV-induced cell death in this model. In addition, some studies reported that DENV and ZIKV may modulate mitophagy, a mitochondria quality control that is also linked to mitochondria morphology and cell survival.[62–64] Overall, this suggests that a functional interplay between mitochondrial morphodynamics, respiratory metabolism, and virus-induced apoptosis dictates the fate of the infected cell.

The studies mentioned above highlight some inconsistencies in the descriptions of mitochondrial morphodynamics and energy consumption during flavivirus infection. Some of these discrepancies may be explained by the used viral strains and/or cell types that are more prone to cell death induction (and metabolism suppression) upon infection/stress (e.g., neurons, immune competent cells). Additionally, we believe that our kinetic analysis described here demonstrates that the time of infection (and most probably the extent of viral protein and remodeled organelles accumulation) is an important determinant of flaviviral impact on respiratory metabolism, which may partly explain these discrepancies. Furthermore, we used here Huh7.5 cells which are deficient in RIG-I-dependent signaling and interferon production. Thus, we can rule out that the observed phenotypes of this study are due to the activation of antiviral innate immunity. The fact that ERMC protein knockdown increased the oxygen consumption rate (Figures 5A–5C) supports the model in which DENV and ZIKV alter ERMCs to stimulate mitochondrial activity to delay cell death at the late time points of infection and maximize replication. While the flaviviral determinants of ERMC alteration remain unknown, we favor the idea that this morphological remodeling requires the prior ER-related biogenesis of replication organelles *per se* which involves the concerted action of several flaviviral nonstructural proteins.
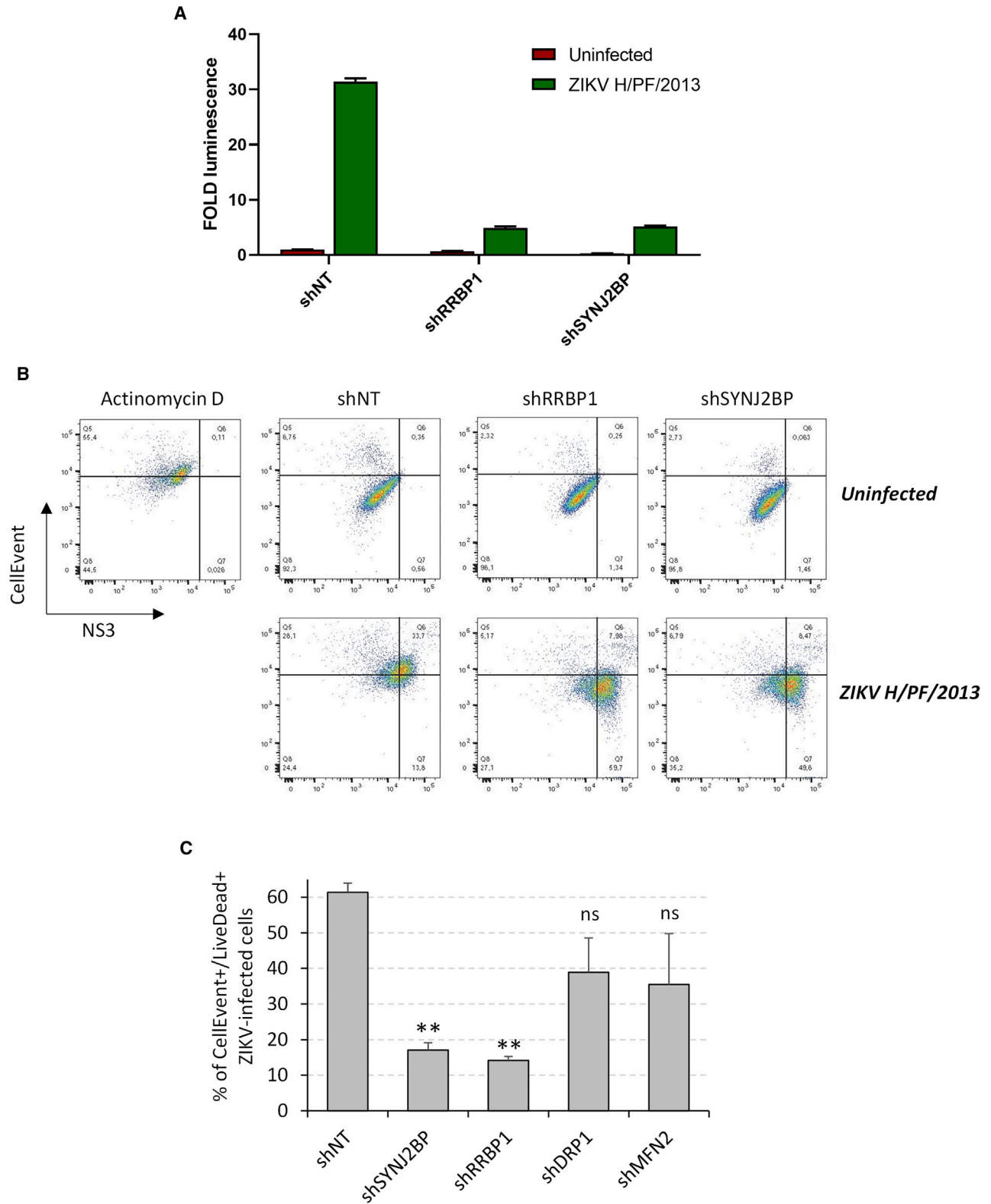
Apoptosis is a programmed cell death that is induced by both extrinsic and intrinsic pathways. This process is most likely induced in flavivirus-infected cells by the massive stress due to the multiple damage-associated molecular patterns resulting from the extensive remodeling and reprogramming of the cytoplasm. However, premature cell death is presumably not optimal for viral replication. The intrinsic apoptosis pathway relies on the activation of caspase 3 through the release of BCL-2 family proteins from mitochondria.[65] Given that ERMCs were reported to regulate this cell death pathway, we investigated whether their alteration could influence ZIKV-induced apoptosis. In this study, we demonstrate that the alteration of ERMCs by knocking down RRBP1 and SYN2BP decreases apoptosis in ZIKV-infected cells (Figure 6). ERMCs notably regulate this cell death induction

(legend on next page)

pathway through IP3R1 and VDAC1 which interact and act as calcium channels to directly transfer calcium from the ER to mitochondria. Since an overload of calcium in mitochondria leads to apoptosis,[66] it is tempting to speculate that the loss of ERMCs reduces the amounts of mitochondrial calcium and thus, delays the induction of apoptosis. Mitochondrial fission positively regulates the activation of apoptosis, notably through the interaction between DRP1 and BAX, a pro-apoptotic factor.[67–70] However, RRBP1 and SYN2JBP knockdown did not result in apparent changes in mitochondria morphology, thus allowing us to conclude that these phenotypes were not related to the mitochondria elongation induced by DENV and ZIKV. Interestingly, we have already shown that the integrity of CMs during ZIKV infection is required to both dampen apoptosis and maintain the elongated morphology of mitochondria.[19] This suggests that both DENV/ZIKV-induced mitochondria elongation and ERMC alteration independently regulate apoptosis. It is interesting to note that in our cell culture system, mitochondria integrity appeared to be preserved upon DENV/ZIKV infection and ERMC protein knockdown since we did not detect any obvious changes in the mitochondrial membrane potential (Figures S6C and S7C).

Finally, the ERMC compartment also serves as a signaling platform during early antiviral innate immunity leading to the induction of type I and III interferons. When RIG-I senses a foreign RNA, it is translocated to the surface of the mitochondria and binds the mitochondrial antiviral-signalling protein adaptor (MAVS) which is located at the ERMC.[32] Several inhibition mechanisms of RIG-I activation by flaviviruses have been discovered in the last decade, notably by inhibiting its TRIM25-and 14-3-3ε-dependent translocation to mitochondria.[16,71–77] Thus, perturbing the reticulo-mitochondrial interface may constitute another strategy to inhibit or delay cellular processes that could be harmful for flaviviruses. Interestingly, such a mechanism to dampen RIG-I-dependent innate immune signaling was already shown for the influenza virus which belongs to another virus family.[35] We can rule out the possibility that our phenotypes in RIG-I-deficient Huh7.5 cells are due to interferon induction. Given that flavivirus replication was enhanced in human primary monocytes upon RRBP1 and SYNJ2BP knockdown, it will be interesting to evaluate in future studies whether the alteration of ERMCs by flaviviruses contributes to countering antiviral immunity in immune-competent cells in addition to cell death.

Overall, our data demonstrate that the morphological perturbations of the ERMCs by DENV and ZIKV modulate mitochondrial respiratory metabolism to sustain the energetic needs of the flaviviral life cycle. This study further supports a model in which these viruses perturb ERMC to hijack specific host factors that are required for CM morphogenesis, and vice-versa. More studies are required to better understand these mechanisms at a molecular level, including the specific viral determinants involved in the alteration of ERMCs and mitochondrial respiration. It will be also interesting to evaluate how this impacts mitochondrial functions other than apoptosis and innate immunity, such as calcium homeostasis or lipid metabolism.

Limitations of the study

In the study, we show that ZIKV and DENV infections alter endoplasmic-reticulum-mitochondria contact sites. However, the molecular mechanisms underlying this morphological remodeling remain poorly characterized. First, although such an alteration correlates with changes in the profile of tethering proteins RRBP1 and SYNJ2BP in infected cells, future studies will have to address whether these two phenotypes are mechanistically linked. This includes investigating whether the ZIKV-induced SYNJ2BP product results from posttranslational modifications of SYNJ2BP or from messenger RNA (mRNA) splicing-related expression of an additional SYNJ2BP isoform. In any case, it would be highly relevant to assess the impact of overexpressing such an alternative SYNJ2BP product or "non-modifiable" mutants on ERMCs stability and viral replication efficiency. In the same line of ideas, is the RRBP1 expression decrease upon infection due to enhanced protein degradation (possibly by NS2B/3 viral protease), and/or to an impairment at the mRNA transcription, stability, or translation level? Second, the viral determinant of the disruption of the reticulo-mitochondrial interface is still unknown. Our repeated attempts failed to link this phenotype to NS4B, a "natural suspect" given its reported capacity to induce mitochondria elongation. Thus, other viral proteins (alone or in combination) might control this process and will have to be assessed in overexpression studies. Answers to these key remaining questions will help to better understand the cytoplasmic remodeling by orthoflaviviruses and may contribute to identifying novel therapeutic targets.

RESOURCE AVAILABILITY

Lead contact

Further information and requests for resources and reagents should be directed to and will be fulfilled by the lead contact, Laurent Chatel-Chaix (Laurent.chatel-chaix@inrs.ca).

Materials availability

This study did not generate new unique reagents.

Figure 6. ERMC alteration dampens ZIKV-induced apoptosis

(A) Huh7.5 cells were transduced with lentiviruses expressing shRNAs which target the indicated proteins (MOI = 4). Two days post-transduction, cells were infected with ZIKV H/PF/2013 (MOI = 20) or left uninfected. Two days post-infection, cell lysates were prepared, and apoptosis induction was measured by measuring bioluminescence using the Caspase-Glo 3/7 assay kit. The showed results are representative of three independent experiments.

(B) Cells were transduced and infected as in (A). Two days post-infection (i.e., 4 days post-transduction), apoptosis induction, cell death, and ZIKV infection were detected by flow cytometry using the CellEvent caspase-3/7 green reagent, the amine reactive viability dye LIVE/DEAD aqua fixable stain, and anti-NS3 antibodies, respectively. Actinomycin D treatment (2.5 μM, 24 h) was used as a positive control of apoptosis induction. The plots show representative results of the caspase activity in function of NS3 expression.

(C) Gated ZIKV-infected cells (i.e., NS3+ cells) were analyzed for apoptosis induction and cell viability using the CellEvent caspase-3/7 green and LIVE/DEAD biosensors, respectively. All values were normalized to the shNT condition. **: $p \leq 0.01$; ns: not significant; one-way ANOVA test; $N = 3$.

DECLARATION OF INTERESTS

The authors declare that they have no conflicts of interest.

STAR★METHODS

Detailed methods are provided in the online version of this paper and include the following:

- KEY RESOURCES TABLE
- EXPERIMENTAL MODEL AND STUDY PARTICIPANT DETAILS
  - Cell lines
  - Primary cell cultures
  - Virus strains
- METHOD DETAILS
  - Antibodies
  - Lentivirus production, titration, and transduction
  - Cell viability assays
  - Renilla luciferase assays
  - Virus production assays
  - Immunofluorescence-based confocal microscopy
  - Proximity ligation assays
  - Transmission electron microscopy
  - Oxygen consumption rate measurements
  - Mitochondria affinity purification and quantitative LC-MS/MS
  - GC-MS metabolomic analyses
  - Human primary monocytes infection
  - Caspase-Glo 3/7 assays
  - Flow cytometry
- QUANTIFICATION AND STATISTICAL ANALYSIS

SUPPLEMENTAL INFORMATION

Supplemental information can be found online at https://doi.org/10.1016/j.isci. 2024.111599.

REFERENCES

1. Bhatt, S., Gething, P.W., Brady, O.J., Messina, J.P., Farlow, A.W., Moyes, C.L., Drake, J.M., Brownstein, J.S., Hoen, A.G., Sankoh, O., et al. (2013). The global distribution and burden of dengue. Nature *496*, 504–507. https://doi.org/10.1038/nature12060.

2. Liu-Helmersson, J., Quam, M., Wilder-Smith, A., Stenlund, H., Ebi, K., Massad, E., and Rocklöv, J. (2016). Climate Change and Aedes Vectors: 21st Century Projections for Dengue Transmission in Europe. EBioMedicine *7*, 267–277. https://doi.org/10.1016/j.ebiom.2016.03.046.

3. Ryan, S.J., Carlson, C.J., Mordecai, E.A., and Johnson, L.R. (2019). Global expansion and redistribution of Aedes-borne virus transmission risk with climate change. PLoS Neglected Trop. Dis. *13*, e0007213. https://doi. org/10.1371/journal.pntd.0007213.

4. WHO (2024). Fact sheets: Dengue and severe dengue. https://www.who. int/news-room/fact-sheets/detail/dengue-and-severe-dengue.

5. Moore, C.A., Staples, J.E., Dobyns, W.B., Pessoa, A., Ventura, C.V., Fonseca, E.B.D., Ribeiro, E.M., Ventura, L.O., Neto, N.N., Arena, J.F., and Rasmussen, S.A. (2017). Characterizing the Pattern of Anomalies in Congenital Zika Syndrome for Pediatric Clinicians. JAMA Pediatr. *171*, 288–295. https://doi.org/10.1001/jamapediatrics.2016.3982.

6. Carod-Artal, F.J. (2018). Neurological complications of Zika virus infection. Expert Rev. Anti Infect. Ther. *16*, 399–410. https://doi.org/10.1080/14787210.2018.1466702.

7. Mazeaud, C., Freppel, W., and Chatel-Chaix, L. (2018). The Multiples Fates of the Flavivirus RNA Genome During Pathogenesis. Front. Genet. 9, 595. https://doi.org/10.3389/fgene.2018.00595.

8. Paul, D., and Bartenschlager, R. (2015). Flaviviridae Replication Organelles: Oh, What a Tangled Web We Weave. Annu. Rev. Virol. 2, 289–310. https://doi.org/10.1146/annurev-virology-100114-055007.

9. Chatel-Chaix, L., and Bartenschlager, R. (2014). Dengue virus- and hepatitis C virus-induced replication and assembly compartments: the enemy inside–caught in the web. J. Virol. 88, 5907–5911. https://doi.org/10.1128/JVI.03404-13.

10. Junjhon, J., Pennington, J.G., Edwards, T.J., Perera, R., Lanman, J., and Kuhn, R.J. (2014). Ultrastructural characterization and three-dimensional architecture of replication sites in dengue virus-infected mosquito cells. J. Virol. 88, 4687–4697. https://doi.org/10.1128/JVI.00118-14.

11. Miorin, L., Romero-Brey, I., Maiuri, P., Hoppe, S., Krijnse-Locker, J., Bartenschlager, R., and Marcello, A. (2013). Three-dimensional architecture of tick-borne encephalitis virus replication sites and trafficking of the replicated RNA. J. Virol. 87, 6469–6481. https://doi.org/10.1128/JVI.03456-12.

12. Gillespie, L.K., Hoenen, A., Morgan, G., and Mackenzie, J.M. (2010). The endoplasmic reticulum provides the membrane platform for biogenesis of the flavivirus replication complex. J. Virol. 84, 10438–10447. https://doi.org/10.1128/JVI.00986-10.

13. Welsch, S., Miller, S., Romero-Brey, I., Merz, A., Bleck, C.K.E., Walther, P., Fuller, S.D., Antony, C., Krijnse-Locker, J., and Bartenschlager, R. (2009). Composition and three-dimensional architecture of the dengue virus replication and assembly sites. Cell Host Microbe 5, 365–375. https://doi.org/10.1016/j.chom.2009.03.007.

14. Cortese, M., Goellner, S., Acosta, E.G., Neufeldt, C.J., Oleksiuk, O., Lampe, M., Haselmann, U., Funaya, C., Schieber, N., Ronchi, P., et al. (2017). Ultrastructural Characterization of Zika Virus Replication Factories. Cell Rep. 18, 2113–2123. https://doi.org/10.1016/j.celrep.2017.02.014.

15. Neufeldt, C.J., and Cortese, M. (2022). Membrane architects: how positive-strand RNA viruses restructure the cell. J. Gen. Virol. 103, 1773. https://doi.org/10.1099/jgv.0.001773.

16. Chatel-Chaix, L., Cortese, M., Romero-Brey, I., Bender, S., Neufeldt, C.J., Fischl, W., Scaturro, P., Schieber, N., Schwab, Y., Fischer, B., et al. (2016). Dengue Virus Perturbs Mitochondrial Morphodynamics to Dampen Innate Immune Responses. Cell Host Microbe 20, 342–356. https://doi.org/10.1016/j.chom.2016.07.008.

17. Miller, S., Kastner, S., Krijnse-Locker, J., Bühler, S., and Bartenschlager, R. (2007). The non-structural protein 4A of dengue virus is an integral membrane protein inducing membrane alterations in a 2K-regulated manner. J. Biol. Chem. 282, 8873–8882. https://doi.org/10.1074/jbc.M609919200.

18. Barbier, V., Lang, D., Valois, S., Rothman, A.L., and Medin, C.L. (2017). Dengue virus induces mitochondrial elongation through impairment of Drp1-triggered mitochondrial fission. Virology 500, 149–160. https://doi.org/10.1016/j.virol.2016.10.022.

19. Anton, A., Mazeaud, C., Freppel, W., Gilbert, C., Tremblay, N., Sow, A.A., Roy, M., Rodrigue-Gervais, I.G., and Chatel-Chaix, L. (2021). Valosin-containing protein ATPase activity regulates the morphogenesis of Zika virus replication organelles and virus-induced cell death. Cell Microbiol. 23, e13302. https://doi.org/10.1111/cmi.13302.

20. El-Bacha, T., Midlej, V., Pereira da Silva, A.P., Silva da Costa, L., Benchimol, M., Galina, A., and Da Poian, A.T. (2007). Mitochondrial and bioenergetic dysfunction in human hepatic cells infected with dengue 2 virus. Biochim. Biophys. Acta 1772, 1158–1166. https://doi.org/10.1016/j.bbadis.2007.08.003.

21. Chen, Q., Gouilly, J., Ferrat, Y.J., Espino, A., Glaziou, Q., Cartron, G., El Costa, H., Al-Daccak, R., and Jabrane-Ferrat, N. (2020). Metabolic reprogramming by Zika virus provokes inflammation in human placenta. Nat. Commun. 11, 2967. https://doi.org/10.1038/s41467-020-16754-z.

22. Ledur, P.F., Karmirian, K., Pedrosa, C.D.S.G., Souza, L.R.Q., Assis-de-Lemos, G., Martins, T.M., Ferreira, J.D.C.C.G., de Azevedo Reis, G.F., Silva, E.S., Silva, D., et al. (2020). Zika virus infection leads to mitochondrial failure, oxidative stress and DNA damage in human iPSC-derived astrocytes. Sci. Rep. 10, 1218. https://doi.org/10.1038/s41598-020-57914-x.

23. Yau, C., Low, J.Z.H., Gan, E.S., Kwek, S.S., Cui, L., Tan, H.C., Mok, D.Z.L., Chan, C.Y.Y., Sessions, O.M., Watanabe, S., et al. (2021). Dysregulated metabolism underpins Zika-virus-infection-associated impairment in fetal development. Cell Rep. 37, 110118. https://doi.org/10.1016/j.celrep.2021.110118.

24. Csordas, G., Renken, C., Varnai, P., Walter, L., Weaver, D., Buttle, K.F., Balla, T., Mannella, C.A., and Hajnoczky, G. (2006). Structural and functional features and significance of the physical linkage between ER and mitochondria. J. Cell Biol. 174, 915–921. https://doi.org/10.1083/jcb.200604016.

25. Vance, J.E. (2015). Phospholipid synthesis and transport in mammalian cells. Traffic 16, 1–18. https://doi.org/10.1111/tra.12230.

26. Fujimoto, M., and Hayashi, T. (2011). New insights into the role of mitochondria-associated endoplasmic reticulum membrane. Int. Rev. Cell Mol. Biol. 292, 73–117. https://doi.org/10.1016/B978-0-12-386033-0.00002-5.

27. Schwarz, D.S., and Blower, M.D. (2016). The endoplasmic reticulum: structure, function and response to cellular signaling. Cell. Mol. Life Sci. 73, 79–94. https://doi.org/10.1007/s00018-015-2052-6.

28. Pourcelot, M., and Arnoult, D. (2014). Mitochondrial dynamics and the innate antiviral immune response. FEBS J. 281, 3791–3802. https://doi.org/10.1111/febs.12940.

29. Cohen, S., Valm, A.M., and Lippincott-Schwartz, J. (2018). Interacting organelles. Curr. Opin. Cell Biol. 53, 84–91. https://doi.org/10.1016/j.ceb.2018.06.003.

30. Friedman, J.R., Lackner, L.L., West, M., DiBenedetto, J.R., Nunnari, J., and Voeltz, G.K. (2011). ER tubules mark sites of mitochondrial division. Science 334, 358–362. https://doi.org/10.1126/science.1207385.

31. Hamasaki, M., Furuta, N., Matsuda, A., Nezu, A., Yamamoto, A., Fujita, N., Oomori, H., Noda, T., Haraguchi, T., Hiraoka, Y., et al. (2013). Autophagosomes form at ER-mitochondria contact sites. Nature 495, 389–393. https://doi.org/10.1038/nature11910.

32. Horner, S.M., Liu, H.M., Park, H.S., Briley, J., and Gale, M., Jr. (2011). Mitochondrial-associated endoplasmic reticulum membranes (MAM) form innate immune synapses and are targeted by hepatitis C virus. Proc. Natl. Acad. Sci. USA 108, 14590–14595. https://doi.org/10.1073/pnas.1110133108.

33. Horner, S.M., Wilkins, C., Badil, S., Iskarpatyoti, J., and Gale, M., Jr. (2015). Proteomic analysis of mitochondrial-associated ER membranes (MAM) during RNA virus infection reveals dynamic changes in protein and organelle trafficking. PLoS One 10, e0117963. https://doi.org/10.1371/journal.pone.0117963.

34. Cook, K.C., Tsopurashvili, E., Needham, J.M., Thompson, S.R., and Cristea, I.M. (2022). Restructured membrane contacts rewire organelles for human cytomegalovirus infection. Nat. Commun. 13, 4720. https://doi.org/10.1038/s41467-022-32488-6.

35. Pila-Castellanos, I., Molino, D., McKellar, J., Lines, L., Da Graca, J., Tauziet, M., Chanteloup, L., Mikaelian, I., Meyniel-Schicklin, L., Codogno, P., et al. (2021). Mitochondrial morphodynamics alteration induced by influenza virus infection as a new antiviral strategy. PLoS Pathog. 17, e1009340. https://doi.org/10.1371/journal.ppat.1009340.

36. Molino, D., Pila-Castellanos, I., Marjault, H.B., Dias Amoedo, N., Kopp, K., Rochin, L., Karmi, O., Sohn, Y.S., Lines, L., Hamaï, A., et al. (2020). Chemical targeting of NEET proteins reveals their function in mitochondrial morphodynamics. EMBO Rep. 21, e49019. https://doi.org/10.15252/embr.201949019.

37. Loo, Y.M., and Gale, M., Jr. (2011). Immune signaling by RIG-I-like receptors. Immunity *34*, 680–692. https://doi.org/10.1016/j.immuni.2011.05.003.

38. Chazal, M., Beauclair, G., Gracias, S., Najburg, V., Simon-Lorière, E., Tangy, F., Komarova, A.V., and Jouvenet, N. (2018). RIG-I Recognizes the 5' Region of Dengue and Zika Virus Genomes. Cell Rep. *24*, 320–328. https://doi.org/10.1016/j.celrep.2018.06.047.

39. De Vos, K.J., Mórotz, G.M., Stoica, R., Tudor, E.L., Lau, K.F., Ackerley, S., Warley, A., Shaw, C.E., and Miller, C.C.J. (2012). VAPB interacts with the mitochondrial protein PTPIP51 to regulate calcium homeostasis. Hum. Mol. Genet. *21*, 1299–1311. https://doi.org/10.1093/hmg/ddr559.

40. Hung, V., Lam, S.S., Udeshi, N.D., Svinkina, T., Guzman, G., Mootha, V.K., Carr, S.A., and Ting, A.Y. (2019). Correction: Proteomic mapping of cytosol-facing outer mitochondrial and ER membranes in living human cells by proximity biotinylation. Elife 8, e50707. https://doi.org/10.7554/eLife.50707.

41. Duan, Y., Wang, X., Sun, K., Lin, Y., Wang, X., Chen, K., Yang, G., Wang, X., and Du, C. (2022). SYNJ2BP Improves the Production of Lentiviral Envelope Protein by Facilitating the Formation of Mitochondrion-Associated Endoplasmic Reticulum Membrane. J. Virol. *96*, e0054922. https://doi.org/10.1128/jvi.00549-22.

42. Hartmann, J., and Verkhratsky, A. (1998). Relations between intracellular Ca2+ stores and store-operated Ca2+ entry in primary cultured human glioblastoma cells. J. Physiol. *513*, 411–424. https://doi.org/10.1111/j.1469-7793.1998.411bb.x.

43. Anastasia, I., Ilacqua, N., Raimondi, A., Lemieux, P., Ghandehari-Alavijeh, R., Faure, G., Mekhedov, S.L., Williams, K.J., Caicci, F., Valle, G., et al. (2021). Mitochondria-rough-ER contacts in the liver regulate systemic lipid homeostasis. Cell Rep. *34*, 108873. https://doi.org/10.1016/j.celrep.2021.108873.

44. Stoica, R., De Vos, K.J., Paillusson, S., Mueller, S., Sancho, R.M., Lau, K.F., Vizcay-Barrena, G., Lin, W.L., Xu, Y.F., Lewis, J., et al. (2014). ER-mitochondria associations are regulated by the VAPB-PTPIP51 interaction and are disrupted by ALS/FTD-associated TDP-43. Nat. Commun. *5*, 3996. https://doi.org/10.1038/ncomms4996.

45. Deng, L., Adachi, T., Kitayama, K., Bungyoku, Y., Kitazawa, S., Ishido, S., Shoji, I., and Hotta, H. (2008). Hepatitis C virus infection induces apoptosis through a Bax-triggered, mitochondrion-mediated, caspase 3-dependent pathway. J. Virol. *82*, 10375–10385. https://doi.org/10.1128/JVI.00395-08.

46. Duan, X., Li, S., Holmes, J.A., Tu, Z., Li, Y., Cai, D., Liu, X., Li, W., Yang, C., Jiao, B., et al. (2018). MicroRNA 130a Regulates both Hepatitis C Virus and Hepatitis B Virus Replication through a Central Metabolic Pathway. J. Virol. *92*, e02009-17. https://doi.org/10.1128/JVI.02009-17.

47. Deng, Y.Q., Zhang, N.N., Li, C.F., Tian, M., Hao, J.N., Xie, X.P., Shi, P.Y., and Qin, C.F. (2016). Adenosine Analog NITD008 Is a Potent Inhibitor of Zika Virus. Open Forum Infect. Dis. *3*, ofw175. https://doi.org/10.1093/ofid/ofw175.

48. Sow, A.A., Pahmeier, F., Ayotte, Y., Anton, A., Mazeaud, C., Charpentier, T., Angelo, L., Woo, S., Cerikan, B., Falzarano, D., et al. (2023). N-Phenyl-pyridine-3-Carboxamide and 6-Acetyl-1H-Indazole Inhibit the RNA Replication Step of the Dengue Virus Life Cycle. Antimicrob. Agents Chemother. *67*, e0133122. https://doi.org/10.1128/aac.01331-22.

49. Giamogante, F., Poggio, E., Barazzuol, L., Covallero, A., and Calì, T. (2021). Apoptotic signals at the endoplasmic reticulum-mitochondria interface. Adv. Protein Chem. Struct. Biol. *126*, 307–343. https://doi.org/10.1016/bs.apcsb.2021.02.007.

50. Suresh, S.N. (2019). Endoplasmic reticulum mitochondria contacts modulate apoptosis of renal cells and its implications in diabetic neuropathy. EBioMedicine *44*, 24–25. https://doi.org/10.1016/j.ebiom.2019.05.061.

51. Carpio, M.A., Means, R.E., Brill, A.L., Sainz, A., Ehrlich, B.E., and Katz, S.G. (2021). BOK controls apoptosis by Ca(2+) transfer through ER-mitochondrial contact sites. Cell Rep. *34*, 108827. https://doi.org/10.1016/j.celrep.2021.108827.

52. Verfaillie, T., Rubio, N., Garg, A.D., Bultynck, G., Rizzuto, R., Decuypere, J.P., Piette, J., Linehan, C., Gupta, S., Samali, A., and Agostinis, P. (2012). PERK is required at the ER-mitochondrial contact sites to convey apoptosis after ROS-based ER stress. Cell Death Differ. *19*, 1880–1891. https://doi.org/10.1038/cdd.2012.74.

53. Colombini, M. (2016). The VDAC channel: Molecular basis for selectivity. Biochim. Biophys. Acta *1863*, 2498–2502. https://doi.org/10.1016/j.bbamcr.2016.01.019.

54. Gomez-Suaga, P., Paillusson, S., Stoica, R., Noble, W., Hanger, D.P., and Miller, C.C.J. (2017). The ER-Mitochondria Tethering Complex VAPB-PTPIP51 Regulates Autophagy. Curr. Biol. *27*, 371–385. https://doi.org/10.1016/j.cub.2016.12.038.

55. Yeo, H.K., Park, T.H., Kim, H.Y., Jang, H., Lee, J., Hwang, G.S., Ryu, S.E., Park, S.H., Song, H.K., Ban, H.S., et al. (2021). Phospholipid transfer function of PTPIP51 at mitochondria-associated ER membranes. EMBO Rep. *22*, e51323. https://doi.org/10.15252/embr.202051323.

56. Jang, W., Puchkov, D., Samsó, P., Liang, Y., Nadler-Holly, M., Sigrist, S.J., Kintscher, U., Liu, F., Mamchaoui, K., Mouly, V., and Haucke, V. (2022). Endosomal lipid signaling reshapes the endoplasmic reticulum to control mitochondrial function. Science *378*, eabq5209. https://doi.org/10.1126/science.abq5209.

57. Cerikan, B., Goellner, S., Neufeldt, C.J., Haselmann, U., Mulder, K., Chatel-Chaix, L., Cortese, M., and Bartenschlager, R. (2020). A Non-Replicative Role of the 3' Terminal Sequence of the Dengue Virus Genome in Membranous Replication Organelle Formation. Cell Rep. *32*, 107859. https://doi.org/10.1016/j.celrep.2020.107859.

58. Freyre, C.A.C., Rauher, P.C., Ejsing, C.S., and Klemm, R.W. (2019). MIGA2 Links Mitochondria, the ER, and Lipid Droplets and Promotes De Novo Lipogenesis in Adipocytes. Mol. Cell *76*, 811–825.e14. https://doi.org/10.1016/j.molcel.2019.09.011.

59. Janer, A., Morris, J.L., Krols, M., Antonicka, H., Aaltonen, M.J., Lin, Z.Y., Anand, H., Gingras, A.C., Prudent, J., and Shoubridge, E.A. (2024). ESYT1 tethers the ER to mitochondria and is required for mitochondrial lipid and calcium homeostasis. Life Sci. Alliance *7*, e202302335. https://doi.org/10.26508/lsa.202302335.

60. Song, M.H., Sun, Y., and Qiu, X.B. (2024). Hijacking autophagy for infection by flaviviruses. Virus Res. *347*, 199422. https://doi.org/10.1016/j.virusres.2024.199422.

61. Yang, S., Gorshkov, K., Lee, E.M., Xu, M., Cheng, Y.S., Sun, N., Soheilian, F., de Val, N., Ming, G., Song, H., et al. (2020). Zika Virus-Induced Neuronal Apoptosis via Increased Mitochondrial Fragmentation. Front. Microbiol. *11*, 598203. https://doi.org/10.3389/fmicb.2020.598203.

62. Ponia, S.S., Robertson, S.J., McNally, K.L., Subramanian, G., Sturdevant, G.L., Lewis, M., Jessop, F., Kendall, C., Gallegos, D., Hay, A., et al. (2021). Mitophagy antagonism by ZIKV reveals Ajuba as a regulator of PINK1 signaling, PKR-dependent inflammation, and viral invasion of tissues. Cell Rep. *37*, 109888. https://doi.org/10.1016/j.celrep.2021.109888.

63. Singh, B., Avula, K., Sufi, S.A., Parwin, N., Das, S., Alam, M.F., Samantaray, S., Bankapalli, L., Rani, A., Poornima, K., et al. (2022). Defective Mitochondrial Quality Control during Dengue Infection Contributes to Disease Pathogenesis. J. Virol. *96*, e0082822. https://doi.org/10.1128/jvi.00828-22.

64. Lee, J.K., and Shin, O.S. (2023). Zika virus modulates mitochondrial dynamics, mitophagy, and mitochondria-derived vesicles to facilitate viral replication in trophoblast cells. Front. Immunol. *14*, 1203645. https://doi.org/10.3389/fimmu.2023.1203645.

65. Elmore, S. (2007). Apoptosis: a review of programmed cell death. Toxicol. Pathol. *35*, 495–516. https://doi.org/10.1080/01926230701320337.

66. Orrenius, S., Zhivotovsky, B., and Nicotera, P. (2003). Regulation of cell death: the calcium-apoptosis link. Nat. Rev. Mol. Cell Biol. *4*, 552–565. https://doi.org/10.1038/nrm1150.

67. Jenner, A., Peña-Blanco, A., Salvador-Gallego, R., Ugarte-Uribe, B., Zollo, C., Ganief, T., Bierlmeier, J., Mund, M., Lee, J.E., Ries, J., et al. (2022).

DRP1 interacts directly with BAX to induce its activation and apoptosis. EMBO J. *41*, e108587. https://doi.org/10.15252/embj.2021108587.

68. Montessuit, S., Somasekharan, S.P., Terrones, O., Lucken-Ardjomande, S., Herzig, S., Schwarzenbacher, R., Manstein, D.J., Bossy-Wetzel, E., Basañez, G., Meda, P., and Martinou, J.C. (2010). Membrane remodeling induced by the dynamin-related protein Drp1 stimulates Bax oligomerization. Cell *142*, 889–901. https://doi.org/10.1016/j.cell.2010.08.017.

69. Oettinghaus, B., D'Alonzo, D., Barbieri, E., Restelli, L.M., Savoia, C., Licci, M., Tolnay, M., Frank, S., and Scorrano, L. (2016). DRP1-dependent apoptotic mitochondrial fission occurs independently of BAX, BAK and APAF1 to amplify cell death by BID and oxidative stress. Biochim. Biophys. Acta *1857*, 1267–1276. https://doi.org/10.1016/j.bbabio.2016.03.016.

70. Park, J.H., Ko, J., Hwang, J., and Koh, H.C. (2015). Dynamin-related protein 1 mediates mitochondria-dependent apoptosis in chlorpyrifos-treated SH-SY5Y cells. Neurotoxicology *51*, 145–157. https://doi.org/10.1016/j.neuro.2015.10.008.

71. Gack, M.U., and Diamond, M.S. (2016). Innate immune escape by Dengue and West Nile viruses. Curr. Opin. Virol. *20*, 119–128. https://doi.org/10.1016/j.coviro.2016.09.013.

72. Serman, T.M., and Gack, M.U. (2019). Evasion of Innate and Intrinsic Antiviral Pathways by the Zika Virus. Viruses *11*, 970. https://doi.org/10.3390/v11100970.

73. Tremblay, N., Freppel, W., Sow, A.A., and Chatel-Chaix, L. (2019). The Interplay between Dengue Virus and the Human Innate Immune System: A Game of Hide and Seek. Vaccines *7*, 145. https://doi.org/10.3390/vaccines7040145.

74. Liu, H.M., Loo, Y.M., Horner, S.M., Zornetzer, G.A., Katze, M.G., and Gale, M., Jr. (2012). The mitochondrial targeting chaperone 14-3-3epsilon regulates a RIG-I translocon that mediates membrane association and innate antiviral immunity. Cell Host Microbe *11*, 528–537. https://doi.org/10.1016/j.chom.2012.04.006.

75. Riedl, W., Acharya, D., Lee, J.H., Liu, G., Serman, T., Chiang, C., Chan, Y.K., Diamond, M.S., and Gack, M.U. (2019). Zika Virus NS3 Mimics a Cellular 14-3-3-Binding Motif to Antagonize RIG-I- and MDA5-Mediated Innate Immunity. Cell Host Microbe *26*, 493–503.e6. https://doi.org/10.1016/j.chom.2019.09.012.

76. Gack, M.U., Shin, Y.C., Joo, C.H., Urano, T., Liang, C., Sun, L., Takeuchi, O., Akira, S., Chen, Z., Inoue, S., and Jung, J.U. (2007). TRIM25 RING-finger E3 ubiquitin ligase is essential for RIG-I-mediated antiviral activity. Nature *446*, 916–920. https://doi.org/10.1038/nature05732.

77. Manokaran, G., Finol, E., Wang, C., Gunaratne, J., Bahl, J., Ong, E.Z., Tan, H.C., Sessions, O.M., Ward, A.M., Gubler, D.J., et al. (2015). Dengue subgenomic RNA binds TRIM25 to inhibit interferon expression for epidemiological fitness. Science *350*, 217–221. https://doi.org/10.1126/science.aab3369.

78. Freppel, W., Mazeaud, C., and Chatel-Chaix, L. (2018). Production, Titration and Imaging of Zika Virus in Mammalian Cells. Bio. Protoc. *8*, e3115. https://doi.org/10.21769/BioProtoc.3115.

79. Fischl, W., and Bartenschlager, R. (2013). High-throughput screening using dengue virus reporter genomes. Methods Mol. Biol. *1030*, 205–219. https://doi.org/10.1007/978-1-62703-484-5_17.

80. Mazeaud, C., Anton, A., Pahmeier, F., Sow, A.A., Cerikan, B., Freppel, W., Cortese, M., Bartenschlager, R., and Chatel-Chaix, L. (2021). The Biogenesis of Dengue Virus Replication Organelles Requires the ATPase Activity of Valosin-Containing Protein. Viruses *13*, 2092. https://doi.org/10.3390/v13102092.

81. Scaturro, P., Stukalov, A., Haas, D.A., Cortese, M., Draganova, K., Płaszczyca, A., Bartenschlager, R., Götz, M., and Pichlmair, A. (2018). An orthogonal proteomic survey uncovers novel Zika virus host factors. Nature *561*, 253–257. https://doi.org/10.1038/s41586-018-0484-5.

82. Tyanova, S., Temu, T., and Cox, J. (2016). The MaxQuant computational platform for mass spectrometry-based shotgun proteomics. Nat. Protoc. *11*, 2301–2319. https://doi.org/10.1038/nprot.2016.136.

83. Holze, C., Michaudel, C., Mackowiak, C., Haas, D.A., Benda, C., Hubel, P., Pennemann, F.L., Schnepf, D., Wettmarshausen, J., Braun, M., et al. (2018). Oxeiptosis, a ROS-induced caspase-independent apoptosis-like cell-death pathway. Nat. Immunol. *19*, 130–140. https://doi.org/10.1038/s41590-017-0013-y.

84. Tyanova, S., Temu, T., Sinitcyn, P., Carlson, A., Hein, M.Y., Geiger, T., Mann, M., and Cox, J. (2016). The Perseus computational platform for comprehensive analysis of (prote)omics data. Nat. Methods *13*, 731–740. https://doi.org/10.1038/nmeth.3901.

85. Hulea, L., Gravel, S.P., Morita, M., Cargnello, M., Uchenunu, O., Im, Y.K., Lehuede, C., Ma, E.H., Leibovitch, M., McLaughlan, S., et al. (2018). Translational and HIF-1alpha-Dependent Metabolic Reprogramming Underpin Metabolic Plasticity and Responses to Kinase Inhibitors and Biguanides. Cell Metabol. *28*, 817–832. https://doi.org/10.1016/j.cmet.2018.09.001.

STAR★METHODS

KEY RESOURCES TABLE

REAGENT or RESOURCE	SOURCE	IDENTIFIER
Antibodies		
Rabbit anti-DENV NS4B	GeneTex	GTX124250
Rabbit anti-ZIKV NS4B	GeneTex	GTX133311
Rabbit anti-ZIKV NS3	GeneTex	GTX133309
Mouse monoclonal anti-DENV NS3	GeneTex	GTX629477
Rat polyclonal antibodies against DENV2 16681 NS3	Not commercial, produced by Medimabs	reported before (Anton et al., 2021)
Mouse anti-VDAC1	Abcam	ab14734
Mouse anti-GRP75	Abcam	ab2799
Rabbit anti-IP3R1	Novus Biologicals	NBP2-22458
Mouse anti-VAPB	ProteinTech	66191-1-Ig
Mouse anti-RRBP1	Invitrogen	MA5-18302
Rabbit anti-PTPIP51	Sigma-Millipore	HPA009975
Rabbit anti-SYNJ2BP	Sigma-Millipore	HPA000866
Rabbit anti-TOM20	Cell Signaling Technology	42406
Rabbit anti-SDHAF2	RayBiotech	144-64204
Bacterial and virus strains		
ZIKV H/PF/2013	European Virus Archive Global	N/A
ZIKV MR766	European Virus Archive Global	N/A
DENV2 16681s	(Fischl & Bartenschlager, 2013)	N/A
Rluc-expressing DENV-R2A	(Fischl & Bartenschlager, 2013)	N/A
Chemicals, peptides, and recombinant proteins		
NITD008	Tocris Small Molecules	6045/1
Deposited data		
Proteomics	ProteomeXchange	PXD057947
Metabolomics	Mendeley Data	6yvtysrwfv.1
Experimental models: Cell lines		
Huh7.5	Gift from Patrick Labonté (INRS)	N/A
Vero E6	ATCC	CRL-1586
JEG-3	ATCC	HTB-36
A549	ATCC	CCL-185
HEK293T	Gift from Frédérick-Antoine Mallette (University of Montreal)	N/A
HeLa	Gift from Frédérick-Antoine Mallette (University of Montreal)	N/A
Software and algorithms		
Fiji	ImageJ.net	version 2.16.0
GraphPad Prism 8	Graphpad	version 8.0.1
MaxQuant	Jürgen Cox Laboratory; https://www.biochem.mpg.de/6304115/maxquant	version 1.5.6.2
Perseus	Jürgen Cox Laboratory; https://www.biochem.mpg.de/6304220/perseus	version 1.6.10.43
Chemstation	Agilent, Santa Clara, USA	N/A
MassHunter	Agilent, Santa Clara, USA	N/A
Wave	Agilent, Santa Clara, USA	version 2.6.1
FlowJo	BD	version 10.0
Image Lab	Bio-Rad	version 5.0

(*Continued on next page*)

Continued

REAGENT or RESOURCE	SOURCE	IDENTIFIER
Other		
Mission shSYNJ2BP	Millipore Sigma	TRCN0000121988
Mission shRRBP1	Millipore Sigma	TRCN0000117408
Mission shVAPB	Millipore Sigma	TRCN0000152520
Mission shPTPIP51	Millipore Sigma	TRCN0000135580
Mission shDRP1	Millipore Sigma	TRCN0000001097
Mission shMFN2	Millipore Sigma	TRCN0000082686

EXPERIMENTAL MODEL AND STUDY PARTICIPANT DETAILS

Cell lines

Huh7.5 (Human, male), A549 (Human, male), HEK293T (Human female), VeroE6 (African green monkey, female), and HeLa (Human, female) cells were cultured in Dulbecco's modified Eagle medium (DMEM, Life Technologies) supplemented with 10% fetal bovine serum (FBS, Wisent), 1% non-essential amino acids (Life Technologies) and 1% penicillin-streptomycin (Life Technologies). JEG-3 cells (Human, female) were cultured in Eagle's minimum essential medium (EMEM, with Earle's salts, Wisent) supplemented as described above for DMEM. Huh7.5 cells stably expressing mito-mTurquoise2 were produced exactly as before using lentiviral transduction[16] and were maintained in 5 μg/mL zeocin (Life Technologies). VeroE6, JEG-3 and A549 cells were obtained from ATCC. The identity of HEK293T and HeLa cells has been confirmed by the short tandem repeats (SRT) profiling authentication method at Génome Québec (Montreal, Canada). The other cell lines were not authenticated. All cell lines were systematically and regularly tested for the absence of mycoplasma contamination with the PCR Mycoplasma Detection Kit (#G238 (AG); Applied Biological Mat. Inc.).

Primary cell cultures

Human peripheral blood mononuclear cells (PBMC) were isolated from venous blood obtained from female healthy volunteers by centrifugation over Ficoll-Paque. Blood donations were obtained from informed and consenting individuals, as per institutionally approved procedures (INRS ethic protocol #CER-15-397). All donors were 20 to 60-year-old non-smokers and have not taken anti-inflammatory drugs for the last 10 days before the experiments. Information related to ancestry, race, or ethnicity is not available. Samples were processed within 30 minutes of blood collection. Upon isolation, PBMCs were counted, and cell viability was assessed using trypan blue exclusion before starting experiments. For monocyte isolation, 1 mL of a 10^6/mL PBMC suspension was added to 6-well plates. The PBMCs were incubated at 37°C in a 5% CO_2 atmosphere for 2 hours in RPMI 1640 medium, 10% FBS, 10 mM HEPES, and 1% penicillin/streptomycin. The supernatant, containing nonadherent PBMCs, was removed, and adherent monocytes were washed twice before lentivirus transduction.

Virus strains

ZIKV H/PF/2013 and ZIKV MR766 strains were provided by the European Virus Archive Global (EVAg). Virus stocks were generated by amplification in VeroE6 cells following inoculation with a multiplicity of infection (MOI) of 0.001. Virus aliquots were stored at 80°C until use. Infectious titers were determined by plaque assays exactly as reported before.[78] DENV2 16681s and reporter Rluc-expressing DENV-R2A particles were generated using a reverse genetics system (a kind gift of Ralf Bartenschlager)[79] and by electroporating VeroE6 cells with *in vitro*-transcribed DENV RNA genomes as reported before.[80]

METHOD DETAILS

Antibodies

Rabbit anti-DENV NS4B (GTX124250; cross-reactive for ZIKV), rabbit anti-ZIKV NS4B (GTX133311), rabbit anti-ZIKV NS3 (GTX133309) and mouse monoclonal anti-DENV NS3 (GTX629477; cross-reactive for ZIKV) were obtained from Genetex. Rat polyclonal antibodies against DENV2 16681 NS3 which are cross-reactive with ZIKV NS3 were generated by Medimabs (Montreal, Canada) as reported before.[19] Mouse anti-VDAC1 (ab14734) and mouse anti-GRP75 (ab2799) were obtained from Abcam. Rabbit anti-IP3R1 (NBP2-22458) antibodies were obtained from Novus Biologicals. Mouse anti-VAPB (66191-1-Ig) was obtained from ProteinTech. Mouse anti-RRBP1 (MA5-18302) was obtained from Invitrogen. Rabbit anti-PTPIP51 (HPA009975) and rabbit anti-SYNJ2BP (HPA000866) were obtained from Sigma-Millipore. Rabbit anti-TOMM20 (42406) and anti-SDHAF2 (144-64204) antibodies were purchased at Cell Signaling Technology and RayBiotech, respectively.

Lentivirus production, titration, and transduction

Knockdowns of ERMC proteins were achieved by transduction with lentiviruses expressing MISSION shRNA from MilliporeSigma (shSYNJ2BP: TRCN0000121988; shRRBP1: TRCN0000117408; shVAPB: TRCN0000152520; shPTPIP51: TRCN0000135580). Constructs expressing shDRP1 and shMFN2 were already described.[16] For lentivirus production, HEK293T cells were transfected with packaging plasmids pCMV-Gag-Pol, pMD2-VSV-G and pLKO-shRNA using 25 kDa linear polyethylenimine (Polysciences Inc.) exactly as before.[16,19,80] Two days post-transfection, lentivirus-containing medium was collected, filtered and stored at -80°C until use. Lentivirus titration was performed in HeLa cells. Cells were seeded at 50,000 cells/well in 24-well plates and lentivirus-containing medium was titrated in 10-fold serial dilutions (10^{-1} to 10^{-3}, in duplicate). Transduced cells were selected one-day post-transduction treatment with 1 μg/mL puromycin. Six days post-transduction, cells were washed once in PBS, and then fixed and stained with 1% crystal violet/10% ethanol for 20 minutes. Stained cells were washed with tap water. Colony-forming units were counted, and titers were determined taking into consideration the dilution factor. Huh7.5 cells were transduced with lentiviruses at a MOI of 5-10 in the presence of 8 μg/mL polybrene.

Cell viability assays

7,500 Huh7.5 cells/well in 100 μl of DMEM were seeded in 96-well plates and transduced as indicated above. Four days post transduction, 20 μL of 3-(4,5-dimethylthiazol-2-yl)-2,5-diphenyltetrazolium bromide (MTT) at 5 mg/mL were added to the medium for 1 to 4 hr at 37°C. Medium was removed and 150 μL of 2% (v/v) of 0.1 M glycine in DMSO (pH 11) were added to dissolve the MTT precipitates. Absorbance at 570 nm was read with Spark multimode microplate reader (Tecan).

Renilla luciferase assays

1.10^5 Huh7.5 cells/well were plated in 12-well plates in triplicates and transduced as indicated above. The day after, the culture medium was replaced. Two days post-transduction, cells were infected with virus DENV-R2A reporter virus (MOI=~0.01). 2 days later, the medium was removed, and cells were lysed in 200 μl of luciferase lysis buffer (1% Triton-X-100; 25 mM Glycyl-Glycine, pH7.8; 15 mM MgSO4; 4 mM EGTA; 1 mM DTT added directly prior to use). 30 μl of lysates were transferred into a white 96-well plate. Luminescence was read with a Spark multimode microplate reader (Tecan) after injection of 150 μl of assay buffer (25 mM Glycyl-Glycine pH7.8; 15 mM KPO4 buffer pH7.8; 15 mM MgSO4; 4 mM EGTA; 1 mM coelenterazine freshly added before the assay). All values were normalized to the shNT control condition.

Virus production assays

2.10^5 Huh7.5 cells/well were plated in 6-well plates and transduced in the presence of 8 μg/mL polybrene. The day after, culture medium was changed. Two days post-transduction, cells were infected with DENV2 16681s or ZIKV H/PF/2013 (MOI = 0.1). Three hours later, culture medium was changed. Two days post-infection, cell supernatants were collected, filtered at 0.45 μm, and kept at -80°C until use. 2.10^5 VeroE6 cells/well were seeded in 24-well plates. The day after, cells were infected in 10-fold serial virus dilutions (10^{-1} to 10^{-6}) in duplicate in complete DMEM. Three hours post-infection, the medium was removed, and replaced with serum-free MEM (Life Technologies) containing 1.5% carboxymethylcellulose (MilliporeSigma). Five (ZIKV) or seven (DENV) days post-infection, cells were fixed for 2 hours in 5% formaldehyde. Cells were washed vigorously with tap water and stained with 1% crystal violet/10% ethanol for 20 minutes. Cells were washed with tap water. Plaques were counted, and infectious titers in particles forming unit (PFU/mL) were calculated.

Immunofluorescence-based confocal microscopy

Huh7.5 cells were seeded on coverslips before immunofluorescence assay and infected the day after with DENV2 16681s (MOI = 1-5) or ZIKV H/PF/2013 (MOI=5-10) 2- or 3-days post-infection, cells were washed three times with PBS and fixed for 20 minutes with PBS containing 4% paraformaldehyde (PFA). Coverslips were rinsed 3 times with PBS and kept at 4°C in PBS until use. Prior immunostaining, cells were permeabilized for 15 min in PBS containing 0.2% Triton X-100, and then blocked for 1hr with PBS containing 5% bovine serum albumin (BSA) and 10% goat serum (Thermo-Fisher). Coverslips were incubated 2 hours with primary antibodies at room temperature diluted in PBS/5% BSA. Coverslips were washed three times in PBS and incubated for 1hr at room temperature and in the dark with Alexa Fluor (488, 568 or 647)-conjugated secondary antibodies (Life Technologies) diluted in PBS/5% BSA. Coverslips were washed three times in PBS and incubated 15 min in PBS containing 4', 6'-diamidino-2-phenylindole (DAPI; Life Technologies) diluted 1/10,000 for nuclei staining. Coverslips were washed three times in PBS, and once in water before being mounted on slides with FluoromountG (Southern Biotechnology Associates). Cells were observed and imaged using a LSM780 confocal microscope (Carl Zeiss Microimaging) at the Confocal Microscopy Core Facility of the INRS-Centre Armand-Frappier Santé Biotechnologie. Images were processed with the Fiji software.

Proximity ligation assays

Huh7.5 cells were cultured on coverslips and infected as above. In the case of JEG-3 and A549 cells, they were infected at a MOI of 1 and processed two days post-infection. Coverslips were washed three times with PBS and fixed for 20 min with PBS/4% PFA. Coverslips were rinsed 3 times with PBS and kept at 4°C in PBS until use. Prior to the assay, cells were permeabilized with 0.2% Triton X-100 for 15 min. Proximity ligation assays were performed using the Duolink PLA Kit (Millipore-Sigma) according to the

manufacturer's protocol. Briefly, cells were blocked with the kit buffer for 1 hr at 37°C in prior incubation with the indicated mouse and rabbit primary antibodies for 2 hours at room temperature. Coverslips were washed three times with the buffer A from the kit and incubated for 1 hr at 37°C with PLUS and MINUS PLA probes. Coverslips were washed three times in buffer A and incubated for 30 min at 37°C with the ligation solution. Coverslips were washed three times with buffer A and incubated 100 min at 37°C with the kit amplification solution. After final washes with buffer B, coverslips were stained as above with rat anti-NS3 antibodies and Alexa Fluor488 anti-rat antibodies (see STAR Methods for immunofluorescence-based confocal microscopy). Cells were then incubated for 15 min in 0.01% buffer B and a 1/10,000 dilution of DAPI (Life Technologies) for nuclei staining. Coverslips were washed three times in buffer B, then once in 0.01% buffer B and mounted on slides with FluoromountG (Southern Biotechnology Associates). Cells were observed and imaged using a LSM780 confocal microscope (Carl Zeiss Microimaging) at the Confocal Microscopy Core Facility of the INRS-Centre Armand-Frappier Santé Biotechnologie. The quantifications of the intracellular PLA dots were performed with the Fiji software. Briefly, 8-bit format images were processed for each channel. We increased the signal for NS3 to saturation in order to delineate the entire cell area. The threshold of PLA signal was adjusted to eliminate the non-specific background. A given PLA signal was considered positive when bigger than $0.02 \mu m^2$ and having a circularity between 0.02 and 1.00. PLA dots were counted in each cell. Same acquisition and counting settings were applied to all data for each experiment.

Transmission electron microscopy

Infected cells were prepared for transmission electron microscopy exactly as previously reported.[19,80] Briefly, Huh7.5 cells were seeded on Lab-tech chambers Slide[TM] (Thermo Fisher) and infected with DENV 16681s MOI 1 or ZIKV H/PF/2013 MOI of 10. Two days later, cells were fixed in 2.5% glutaraldehyde in 0.1M sodium cacodylate buffer pH 7.4 overnight at 4°C and washed three times with washing buffer. Cells were postfixed for 1 hour with the washing buffer containing 1% aqueous OsO_4 and 1.5% aqueous potassium ferrocyanide. Following three washes in washing buffer, samples were dehydrated in sequential dipping into a series of ethanol-dH$_2$O solutions of increasing concentration up to 70% followed by a 1 hour-long staining with 2% uranyl acetate in 70% ethanol. Samples were washed twice in 70% ethanol and subjected to a progressive dehydration with up to 100% ethanol. A Graded Epon-ethanol series (1:1, 3:1) was used to infiltrate the samples before embedding in 100% Epon and polymerizing in an oven at 60°C for 48hrs. A Diatome diamond knife using a Leica Microsystems EM UC7 ultramicrotome was used to cut serial sections (90-100 nm thick) from the polymerized blocks. Ultrathin sections were then transferred into 200-mesh copper grids and stained during 6 minutes with 4% uranyl acetate and 5 minutes in Reynold's lead. Image acquisitions of TEM grids were performed with a FEI Tecnai G2 Spirit 120 kV TEM equipped with a Gatan Ultrascan 4000 CCD Camera Model 895 (Gatan, Pleasanton, CA) located at McGill University Facility for Electron Microscopy Research. TEM images were analyzed using the Fiji software for measurements of mitochondria perimeter and ERMC length in cells from the single sections exhibiting a large cytoplasm (basal side of the cell). Ultrastructures were considered as ERMCs when the measured distance between ER and mitochondria was below 50nm. The ratio between these two values indicated the percentage of the mitochondrial perimeter in contact with ER.

Oxygen consumption rate measurements

The day prior the assay, Seahorse 96-well sensor cartridges (Agilent) were hydrated overnight at 37°C in a non-CO_2 incubator with 200 μl/well of the Seahorse XF calibrant (Agilent). The day of the assay, living cells were trypsinized and counted with Trypan blue. 50,000 cells/well were seeded into a Seahorse XF 96-well cell culture microplate (Agilent) in DMEM and incubated for at least 4 hours at 37°C with 5% CO_2. Culture medium was changed for 180 μl of Seahorse XF DMEM which was supplemented with 1 mM pyruvate, 2 mM glutamine and 10 mM glucose. Cells were incubated for 1 hour in a non-CO_2 incubator at 37°C. For measurements of the oxygen consumption rates, we used the Seahorse XF Cell Mito Stress Test kit (Agilent) according to the manufacturer's instructions. Briefly, 20 μl oligomycin 10 μM, 22 μl FCCP 10 μM and 25 μl rotenone/antimycin A 5 μM were loaded into the ports of the sensor cartridges. Sensor cartridges were placed on top of the Seahorse XF cell culture microplate. Sequential drug addition (10-fold dilution) and time-lapse oxygen consumption rate measurements were achieved with a Seahorse XFe96 analyzer (Agilent). OCR values were obtained using Wave 2.6.1 software (Agilent) to determine the basal respiration, the maximal respiration and the ATP production in each sample. For each experiment, all values from the uninfected and infected conditions were normalized to the average of the first three measures of the OCR in the uninfected or shNT condition (corresponding to the basal respiration, *i.e.*, the average level of mitochondrial respiration in normal conditions). Then, the average and SEM were calculated between three to five independent experiments and plotted using GraphPad Prism 8.0 software.

Mitochondria affinity purification and quantitative LC-MS/MS

For the determination of mitochondrial proteome, four independent affinity purifications were performed for each experimental condition as follows. Huh7.5 cells were infected with DENV2 16681s (MOI=2), ZIKV H/PF/2013 (MOI=10) or ZIKV MR766 (MOI=2) to achieve 100% of infection. Forty hours later, cells were prepared, and mitochondria were purified with the Human Mitochondria Isolation Kit (Miltenyi Biotec) according to the manufacturer's instructions. Briefly, were washed twice with cold PBS and counted. Ten million cells were then lysed with a Dounce homogenizer on ice in the kit lysis buffer supplemented with EDTA-free protease inhibitors (Roche). Cell homogenates were subjected to immunoprecipitation using magnetic beads-coupled anti-TOMM22 antibodies. Isolated mitochondria were centrifuged at 13,000xg for 2 minutes at 4°C and resuspended in in 40 μl U/T buffer (6 M urea, 2 M thiourea, 10 mM Hepes (pH 8.0)), and reduction and alkylation carried out with 10 mM DTT and 55 mM iodoacetamide in 50 mM ABC buffer

(50 mM NH$_4$HCO$_3$ in water pH 8.0), respectively. For the determination of the whole proteome, 5 x 10^6 washed cells were lysed in a buffer containing 6 M guanidium chloride and 10 mM Tris(2-carboxyethyl)phosphine (TCEP), 0.1M Tris/HCl (pH 8). Fifty micrograms of cleared protein lysates were reduced/alkylated and peptides were purified on stage tips as described above After digestion with 1 μg LysC (WAKO Chemicals USA) at room temperature for 3 h, the suspension was diluted in ABC buffer, and the protein solution was digested with trypsin (Promega) overnight at room temperature. Peptides were purified on self-assembled stage tips with three C18 Empore filter discs (3M) and analyzed by liquid chromatography coupled to mass spectrometry on a QExactive HF instrument (Thermo Fisher Scientific) as previously described.[81]

Raw mass-spectrometry data were processed with MaxQuant software versions 1.5.6.2 using the built-in Andromeda search engine to search against the human proteome (*Homo sapiens*; UniprotKB #UP0000005684; release 2012_02) containing forward and reverse sequences concatenated with the DENV (UniprotKB #P29990) and ZIKV (UniprotKB #KU955593) viral proteins, and the label-free quantitation (LFQ) algorithm as described previously.[82,83] Additionally, the intensity-based absolute quantification (iBAQ) algorithm and "Match Between Runs" option were used. In MaxQuant, carbamidomethylation was set as fixed and methionine oxidation and N-acetylation as variable modifications, using an initial mass tolerance of 6 ppm for the precursor ion and 0.5 Da for the fragment ions. Search results were filtered with a false discovery rate (FDR) of 0.01 for peptide and protein identifications.

Perseus software version 1.6.10.43 was used to further process the affinity-purification and global proteome dataset. Protein tables were filtered to eliminate the identifications from the reverse database and common contaminants. In analyzing mass spectrometry data, only proteins identified on the basis of at least one peptide and a minimum of 3 quantitation events in at least one experimental group were considered. Significant interactors were determined by Welch's paired T-tests with permutation-based false discovery rate statistics on LFQ intensities (Global proteomes) or the relative abundance of Mitochondria-enriched proteins after normalization against the corresponding cellular lysates (Mitoproteome) (n=4, (|Log2(fold-change)|) $\geq$ 1.58), -Log10(P-value) $\geq$ 2.). We performed 250 permutations, and the FDR threshold was set at 0.05. The parameter S0 was set at 1 to separate background from specifically enriched interactors (mitoproteome), or to define significantly up- or down-regulated proteins in pairwise comparisons (global proteome).[84] UniprotKB accession codes of protein groups and proteins associated with Krebs cycle and electron transport chain identified by mass spectrometry, and their respective LFQ intensities, normalized ratios and significance values are provided in Table S1. The complete list of identified proteins will be published alongside a different study.

GC-MS metabolomic analyses

For infection experiments, Huh7.5 cells were infected with DENV2 16681s (MOI=2), ZIKV H/PF/2013 (MOI=10) or ZIKV MR766 (MOI=2) to achieve 100% of infection, and collected two days post-infection for metabolite preparation. Briefly, cells were washed on ice three times with a cold and filtered isotonic solution (0.9% NaCl). Cells were then quickly collected with 800 μL of 80% MS-grade methanol which was stored at -80°C. Samples were stored at -80°C until metabolite extraction. In parallel, additional replicate samples were generated for cell counting after trypsinization, and quality controls using western blotting to ensure that the infection was successful. Experiments were designed so that between 0.75 x 10^6 and 2 x 10^6 cells were used for subsequent processing for GC-MS.

Membranes disruption was carried by sonication at 4°C (twice 10 min, 30 sec on, 30 sec off, high setting, Diagenode Bioruptor). Extracts were cleared by centrifugation (15,000 rpm, 10 min, 4°C) and supernatants were transferred into new tubes containing 1μl 800 ng/μl myristic acid-D27 (Sigma; dissolved in pyridine). Next, they were dried in a cold trap (Labconco) overnight at − 4°C. Pellets were solubilized in 30 μl pyridine containing methoxyamine-HCl (10 mg/mL, Sigma) by sonication and vortex, and were incubated at RT for 20 min (methoximation). Samples were centrifuged (15,000 rpm, 10 min, RT) and the supernatants were transferred into glass vials containing MTBSTFA (70 μl, Sigma) for derivatization at 70°C for 1 h. One μL was injected per sample for GC–MS analysis. GC–MS instrumentation and software were all from Agilent. GC–MS methods and analyses are as previously described.[85] Data analyses were performed using the Chemstation and MassHunter software (Agilent, Santa Clara, USA). Three replicates per experiment for each condition were processed. The included data show the mean and SEM obtained from the analysis of 4 independent experiments.

Human primary monocytes infection

PBMC-derived primary monocytes were prepared as described above. Prior to transduction, adherent primary human monocytes in a dedicated well for cell counting were scraped, and the cell suspension was used to determine cell number for calculating the volumes of lentiviruses required to perform a transduction with a multiplicity of infection (MOI) of 5. For transduction, all media were removed, and fresh RPMI 1640 medium, 10% FBS, 10 mM HEPES, and 1% penicillin/streptomycin medium containing 8 μg/mL polybrene and shRNA-expressing lentiviruses were added and incubated overnight at 37°C in a 5% CO$_2$ atmosphere. Subsequently, the cells were gently washed twice with PBS, and fresh medium was added. Two days post-transduction, monocytes were infected with ZIKV H/PF/2013 and DENV2 16681s at a MOI of 1 through antibody-dependent enhancement. For virus-antibody complex formation, virus suspensions were incubated for 30 minutes at 4°C in the presence of 1 μg/mL 4G2 panflaviviral anti-E antibody (Genetex, GTX57154). 1 mL of fresh RPMI containing virus-antibody complexes then added to the well with adherent primary monocytes and incubated at 37°C with 5% CO$_2$ for 2 hours. After the infection, the inoculum was removed, and fresh cell medium was added. As replication control, NS5 inhibitor NITD008 (Tocris Small Molecules) was added at a final concentration of 10μM. One day post-infection, adherent cells were collected and subjected to RNA extraction with the RNeasy mini kit (Qiagen) and RT-qPCR.

Caspase-Glo 3/7 assays

300,000 Huh7.5 cells were seeded in 6-well plates and transduced with shRNA-expressing lentivirus at a MOI of 4 with 8µg/mL poly-brene. Two days post transduction, cells were infected with ZIKV H/PF/2013 (MOI of 20) or left uninfected. Two days post infection, cells were scraped in culture medium, collected, and centrifuged for 1 min at 10,000 rpm. Cell pellets were resuspended in 70 µL of a 50/50% mixture containing PBS and the Caspase-Glo 3/7 reagent (Promega). Lysates were incubated at least 2 hours protected from the light at room temperature. Luminescence was measured in duplicates in white 96-well plates (30 µl/well) with a Spark multi-mode microplate reader (Tecan). All values were background-subtracted and normalized to the shNT-transduced uninfected condition.

Flow cytometry

300,000 Huh7.5 cells were prepared exactly as in Caspase-Glo 3/7 assays. Two days post-infection, cells were detached by trypsin treatment and stained with 25 nM MitoTracker® Orange CM-H_2 TMRos (Thermo-Fisher) for 30 min at 37°C followed by a treatment with 4µM CellEvent caspase 3/7 green (Thermo-Fisher) and the amine reactive viability dye LIVE/DEAD aqua fixable stain (Thermo-Fisher) for 30min in the dark at room temperature. Cells were fixed with 2% formaldehyde and permeabilized with 0.1% Triton X-100. To identify ZIKV-infected cells, total cells were stained for ZIKV using a rat polyclonal anti-NS3 antibodies and subsequently with goat anti-rat cross-adsorbed AlexaFluor 647-conjugated secondary antibodies. Cells were stored at 4°C in the dark until flow cytometry processing (performed within 24 hr) and data acquisition with a BD LSRFortessa instrument at the Flow Cytometry Core Facility of INRS. Data analysis was performed using FlowJo version 10.0 software. After setting of singlets, infected Huh7.5 were defined as NS3+ cells and analyzed for active caspase 3/7 expression and LIVE/DEAD signal.

QUANTIFICATION AND STATISTICAL ANALYSIS

Figures were either plotted in Prism 8.0 or in Microsoft Excel. Images were processed in FIJI and frequently median filtered to reduce noise. For statistics, data were analyzed using GraphPad Prism 8.0 software. Normality test was determined using the D'Agostino & Pearson test. For all figures except Figures 1B and S2B, the significance compared to uninfected controls was determined using either the one-way ANOVA test (with a Dunnett's multiple comparison follow-up test) and the non-parametric Kruskal-Wallis test (with a Dunn's follow-up test) for data presenting a normal distribution and a non-normal distribution, respectively, as specified in legends. For Figure 1B, statistical significance was evaluated with a two-way ANOVA test (with a Dunnett's multiple comparison follow-up test). For Figure S2B, we used the non-parametric Mann–Whitney test. p values < 0.05 were considered significant: ****: $p < 0.0001$; ***: $p < 0.001$; **: $p < 0.01$; *: $p < 0.05$.